Physics of Fluids

On the conservative property of particle-based Fokker–Planck method for rarefied gas flows

Cite as: Phys. Fluids **32**, 127108 (2020); https://doi.org/10.1063/5.0030548
Submitted: 24 September 2020 • Accepted: 12 November 2020 • Published Online: 08 December 2020

Yazhong Jiang (姜亚中) and Chih-Yung Wen (温志湧)

Physics of Fluids ARTICLE scitation.org/journal/phf

On the conservative property of particle-based Fokker–Planck method for rarefied gas flows

Cite as: Phys. Fluids 32, 127108 (2020); doi: 10.1063/5.0030548
Submitted: 24 September 2020 • Accepted: 12 November 2020 •
Published Online: 8 December 2020

Yazhong Jiang (姜亚中)[1] and Chih-Yung Wen (温志湧)[1,2,a)]

AFFILIATIONS

[1] Department of Mechanical Engineering, The Hong Kong Polytechnic University, Kowloon, Hong Kong 999077, China
[2] Interdisciplinary Division of Aeronautical and Aviation Engineering, The Hong Kong Polytechnic University, Kowloon, Hong Kong 999077, China

[a)] **Author to whom correspondence should be addressed:** cywen@polyu.edu.hk

ABSTRACT

The Fokker–Planck-type approximation of the full Boltzmann equation has aroused intense research interest due to its potential for the stochastic particle simulation of rarefied gas flows. The ellipsoidal statistical Fokker–Planck (ES-FP) model treats the evolution of molecular velocity as a continuous stochastic process, and it satisfies the basic requirements for a proper gas-kinetic model including the H-theorem and an adjustable Prandtl number. The ES-FP model can be numerically implemented with computational particles in a Monte Carlo manner. Two different particle ES-FP schemes are presented. The first scheme utilizes the exact stochastic integral solution of the Langevin equations corresponding to the ES-FP equation and couples free-molecular moves and intermolecular collisions. The second scheme is designed to enforce the conservation of momentum and energy during the numerical simulation based on the decoupled algorithm and the analysis of the specific conditions for the conservative property. Numerical tests are conducted to demonstrate the performances of different schemes. In the simulation of a homogeneous gas system, the ES-FP scheme without enforcement of conservation leads to unphysical variation in the momentum and loss in energy, whereas the conservative ES-FP scheme strictly maintains the momentum and energy of the system. For the Mach 6 flows over the leading edge of a flat plate and over a round-nosed blunt body, the non-conservative ES-FP scheme underestimates the shock angle and the shock standoff distance, makes inaccurate predictions of aerodynamic force and heating, and produces low-temperature anomalies in front of the shock waves. In comparison with the results given by the direct simulation Monte Carlo method, the results of the conservative ES-FP simulations show satisfactory accuracy for the flow fields as well as the distributions of pressure, friction, and heat flux on the wall surfaces.

I. INTRODUCTION

The macroscopic governing equations used in continuum gas dynamics lose their validity when they are applied to rarefied gas flows. The degree of rarefaction in a gas flow is indicated by the Knudsen number (Kn), which is defined as the ratio of the mean free path of gas molecules to the characteristic length of the flow. When Kn is not negligibly small, the frequency of intermolecular collisions will be insufficient to maintain the local near-equilibrium state of the gas element, and the distribution function of molecular velocity will significantly deviate from the Maxwellian distribution once it is disturbed. As a consequence, the linear constitutive relation used in the Navier–Stokes equation, the Fourier's law of heat conduction, and the no-slip boundary condition on solid walls are no longer applicable. Typical rarefied flows include the low-density flows encountered in aerospace flights[1–8] and the microscale flows in micro-electro-mechanical systems.[7–14] Such rarefied flows exhibit behaviors beyond the knowledge of continuum flows, and the investigations on these flows must resort to gas-kinetic theory.

The Boltzmann equation[15] provides the theoretical basis for kinetic modeling of dilute gases, and its numerical solution can be obtained by the direct simulation Monte Carlo (DSMC) method.[16,17] Since its inception in the 1960s,[18] the DSMC method has been developed into the mainstream simulation tool for practical rarefied flow problems, especially for the high-speed rarefied gas dynamics. The state of the art in the DSMC developments can be found in Refs. 19–24. By introducing computational particles to represent real gas molecules and utilizing the Monte Carlo technique properly,

the DSMC method reproduces the underlying physics of the Boltzmann equation in a probabilistic manner. Key ideas in the DSMC methods include (1) the decoupling of free-molecular moves and intermolecular collisions over each simulation time step and (2) the pairwise random selection of particles within each grid cell to perform binary collisions. Both physical reasoning and quantitative analysis[25–29] indicate that the grid cell size and the time step in a DSMC simulation must be kept below the kinetic scales in space and time, namely, the mean free path and the mean collision time of gas molecules. Such restrictions make the DSMC method computationally expensive in the low-Knudsen-number flow regime. With the motivation to improve the efficiency of particle-based flow simulations, it is imperative to develop novel kinetic models and corresponding particle algorithms,[30,31] in which the restrictions on the cell size and the time step can be relaxed.

Since the innovative work of Jenny, Torrilhon, and Heinz,[32] a number of investigations on the particle-based Fokker–Planck simulation of gas flows have been carried out during the past decade. In Ref. 32, the Fokker–Planck (FP) kinetic equation is utilized as a simplified model of the full Boltzmann equation. The FP model treats the evolution of individual molecular velocity as a continuous stochastic process, which can be described by the stochastic differential equation (SDE) called the Langevin equation. With a specially designed stochastic integration scheme for the Langevin equation, Jenny *et al.*[32] managed to construct an efficient particle algorithm, which excludes the calculation of intermolecular collisions and therefore offers a possibility of using a coarser computational grid and a larger time step than those used in a DSMC simulation. For the purpose of Prandtl-number correction, modified FP-type kinetic models have been put forward. Gorji *et al.*[33] introduced the cubic FP model so that the correct Prandtl number of monatomic gas Pr = 2/3 can be derived from this kinetic equation. Then, Gorji and Torrilhon[34,35] developed the cubic FP model into the entropic FP model, which satisfies the H-theorem. Other FP models, which satisfy the H-theorem and enable the adjustment of gas Prandtl number, include the modified streaming model[36,37] proposed by Singh and Ansumali[36] as well as the ellipsoidal statistical Fokker–Planck (ES-FP) model due to Mathiaud and Mieussens.[38] Extensions of FP models to multi-species gas mixtures were explored by Gorji and Jenny,[39] Agrawal *et al.*,[40] and Hepp *et al.*[41,42] Besides, various FP models for diatomic and polyatomic gases were constructed by Gorji and Jenny,[43] Mathiaud and Mieussens,[44,45] and Hepp *et al.*[46] Recently, Fokker–Planck-type kinetic modeling for nonequilibrium dense gas and multi-phase flows were investigated by Sadr and Gorji[47] and Sadr *et al.*[48]

In addition to these theoretical modeling works, numerical issues related to the particle Fokker–Planck simulation (also referred to as Langevin dynamics simulation) and its applications have been attracting great interests. Gorji and Jenny[49] modified the original FP algorithm in Refs. 32 and 33. Pfeiffer and Gorji[50] suggested the adaptive particle–cell algorithm in the FP method to further improve the efficiency of the FP method. The intersection of the stochastic molecular path and the computational boundaries were studied in an analytical manner by Zhang and Fan[51] and Önskog and Zhang.[52] Numerical errors in the effective transport properties caused by temporal discretization were analyzed by Zhang *et al.*[53] and Fei *et al.*[54,55] using the Green–Kubo relations. Gorji *et al.*[56] and Collyer *et al.*[57] applied variance reduction techniques to reduce the noise in the FP simulation of low speed flows. Recently, Jenny *et al.*[58] analyzed the bias error of the FP method. Due to the particle nature of the FP method, it can be conveniently combined with other particle methods. For example, Fei and Fan[59] and Fei *et al.*[60] proposed the diffusive information preservation (D-IP) method, and the hybrid FP-DSMC scheme[61–65] has been studied. The FP method has been applied to numerical investigations of high-speed aerodynamics including the supersonic flow over the leading edge of a flat plate,[66] the supersonic flow past a cylinder,[64,67] the nozzle expansion flow,[68] the re-entry aerodynamics of a slender configuration,[69] and the interior structure of normal shock waves.[70] Simulations of microscale rarefied flows were performed with the FP method, including the flows through a slit and an orifice,[71] the thermally induced gas flow in a ratchet microchannel,[72] and the shear-driven flows in microscale gaps and cavities.[73] Recently, Zhang and Önskog[74] utilized the FP molecular simulation to elucidate the mechanism of the macroscopic Rayleigh–Bénard instability from a microscopic point of view. Using the same approach, Zhang *et al.*[75] numerically studied the instability and the transition to turbulence in the Kolmogorov flow, which provides evidence for capturing large-scale coherent structures through the simulation of molecular motions.

In spite of the advances in developing the FP method, there are still some issues about the numerical implementation, which require further clarification. In fact, the numerical schemes used in the aforementioned FP particle simulations can be classified into two distinct categories, hereafter called the coupled schemes and the decoupled schemes. References 32, 33, 51–55, 57–60, and 66 adopted the coupled schemes, in which free-molecular moves and intermolecular collisions are coupled. In a coupled scheme, the position and the velocity of a particle are updated simultaneously using the exact stochastic integral solution of the Langevin equation. By following the treatment of Jenny *et al.*,[32] the tortuosity and randomness of the particle trajectory as well as the correlation between the velocity change and displacement are preserved in every evolution step of the coupled scheme. In contrast, Refs. 41–43, 46, 49, 50, 56, 61–65, and 67–75 adopted the decoupled schemes, in which free-molecular moves and intermolecular collisions are decoupled. In a decoupled scheme, the particle position is simply updated by the free-flight formula, which is linear and deterministic. The velocity updating is performed after the particle move procedure has been finished. For a FP-type particle simulation, the adoption of a coupled scheme or a decoupled scheme will have fundamental influences on its numerical properties, including the conservation of momentum and energy.

The conservative property is crucial to both continuum-based and particle-based flow simulations. In this respect, the success of the DSMC method is largely due to the calculation of each binary collision with intrinsic conservation.[16] For the original FP method, the conservation of momentum and energy is true only in a statistical sense, without a guarantee at the numerical level. However, for the decoupled FP schemes, there have been some remedies to numerically ensure the conservative property. One feasible approach, used by Gorji and Jenny[49] as well as Pfeiffer and Gorji,[50] is to transform the set of random variables for the particle evolution in each computational cell at each time step. The transformation shifts and scales the generated random variables to normalize their mean and variance. Alternatively, another approach is imposed on

the particle velocity directly. For example, Pfeiffer *et al.*[68] and Fei *et al.*[70] added a velocity correction procedure at the end of each time step of their FP simulations. In this correction, velocities of particles in one cell are shifted and scaled so that the conservation of momentum and energy can be enforced. Nevertheless, as a matter of fact, not all aforementioned FP research works paid attention to the conservative property of their FP schemes. Therefore, it is necessary to make detailed numerical comparisons between the performances of conservative and non-conservative FP schemes under various scenarios.

The aims of this work are to study the conservative property of the particle-based FP method and to illustrate the significance of numerical conservation for FP simulations of rarefied gas flows. This paper focuses on the ES-FP kinetic model, which has been studied in Refs. 30, 38, 44, 66, 67, 70, 72, 76, and 77. The numerical implementation of the ES-FP model is based on the previous works of the authors.[66,77] The particle ES-FP scheme of Jiang *et al.*[66] serves as the baseline scheme, and it is developed into a conservative version. Numerical experiments here focus on the high-Mach-number rarefied gas dynamic problems, in which both the flow fields as well as the pressure, friction, and heat flux on wall surfaces are investigated. The remainder of this paper is organized as follows: Kinetic formulation of the ES-FP model is given in Sec. II, followed by a brief review of the particle ES-FP scheme of Jiang *et al.*[66] in Sec. III. Then, Sec. IV elaborates on a different ES-FP scheme that enforces the conservation of momentum and energy. In Sec. V, simulations of a homogeneous system, a flat-plate flow, and a blunt-body flow are considered. The numerical performances of two ES-FP schemes are demonstrated and compared. Finally, conclusions are given in Sec. VI.

II. GAS-KINETIC FOKKER–PLANCK MODEL

The gas-kinetic equation for a single-species monatomic gas describes the evolution of the velocity distribution function $f(t, \boldsymbol{x}, \boldsymbol{c})$ at time t, position $\boldsymbol{x}$, and molecular velocity $\boldsymbol{c}$. If there is no external force field, the gas-kinetic equation has a general form of

$$\frac{\partial f}{\partial t} + c_i \frac{\partial f}{\partial x_i} = S(f), \tag{1}$$

where the second term on the left-hand side is the molecular convection term and the right-hand side $S(f)$ stands for the collision operator. Note that throughout this paper, i, j, and k are tensor indices and follow Einstein's summation convention.

For dilute gases, the widely used Boltzmann equation gives a precise account of binary collisions between molecules with the integral collision operator[15,78]

$$S_{\text{Boltz}}(f) = \int_{\mathbb{R}^3} \int_0^{4\pi} \left[f(\boldsymbol{\zeta}^*) f(\boldsymbol{c}^*) - f(\boldsymbol{\zeta}) f(\boldsymbol{c}) \right] c_r \sigma \mathrm{d}\Omega \, \mathrm{d}\boldsymbol{\zeta}, \tag{2}$$

where $\boldsymbol{c}$ and $\boldsymbol{\zeta}$ are the pre-collision velocities of two colliding molecules, c_r denotes their relative speed $|\boldsymbol{c} - \boldsymbol{\zeta}|$, $\boldsymbol{c}^*$ and $\boldsymbol{\zeta}^*$ are the post-collision velocities, Ω represents the solid angle, and $\sigma \mathrm{d}\Omega$ is the differential collision cross section.

This paper is concerned with an effective approximation of the full Boltzmann equation, named the Fokker–Planck model. With the assumption that the state of a gas molecule $\{\boldsymbol{x}(t), \boldsymbol{c}(t)\}$ is a continuous Markov stochastic process in the phase space, the evolution of the distribution function $f(t, \boldsymbol{x}, \boldsymbol{c})$ can be described by a Fokker–Planck-type equation.[79,80] The general Fokker–Planck equation has the form of Eq. (1) with a differential operator serving as the collision term,

$$S_{\text{FP}}(f) = -\frac{\partial (A_i f)}{\partial c_i} + \frac{1}{2} \frac{\partial^2 (D_{ij} f)}{\partial c_i \partial c_j}, \tag{3}$$

where the first-order derivative term (drift term) contains a drift coefficient vector A_i and the second-order derivative term (diffusion term) contains a diffusion coefficient tensor D_{ij}. Similar to $S_{\text{Boltz}}(f)$, the Fokker–Planck operator $S_{\text{FP}}(f)$ formulates the change rate of the distribution function f due to interactions between molecules. However, instead of the detailed calculation of binary collisions, the Fokker–Planck model describes the effect of molecular interactions as the drift–diffusion process of $f(t, \boldsymbol{x}, \boldsymbol{c})$ over the velocity space. To ensure the consistency between this kinetic model and the macroscopic gas dynamics, the drift coefficient A_i and the diffusion coefficient D_{ij} must be constructed properly. This paper focuses on one of the viable constructions of such A_i and D_{ij}, which results in the ellipsoidal statistical Fokker–Planck (ES-FP) gas-kinetic model equation.[38]

A. Ellipsoidal statistical Fokker–Planck (ES-FP) model

The ES-FP equation for the velocity distribution function $f(t, \boldsymbol{x}, \boldsymbol{c})$ of a single-species monatomic gas can be written as[66]

$$\frac{\partial f}{\partial t} + c_i \frac{\partial f}{\partial x_i} = S_{\text{FP}}^{\text{ES}}(f), \quad S_{\text{FP}}^{\text{ES}}(f) = \frac{1}{\tau} \frac{\partial}{\partial c_i} [(c_i - u_i) f] + \left(\frac{k_{\text{B}} T}{m \tau} \right) E_{ij} \frac{\partial^2 f}{\partial c_i \partial c_j}. \tag{4}$$

In the ES-FP operator, k_{B} is the Boltzmann constant, m denotes the molecular mass, $\boldsymbol{u}(t, \boldsymbol{x})$ is the local gas velocity, $T(t, \boldsymbol{x})$ is the local gas temperature, $\tau(t, \boldsymbol{x})$ is called the relaxation time, and $E_{ij}(t, \boldsymbol{x})$ is a dimensionless tensor that is devised to adjust the gas Prandtl number derived from the ES-FP model. The tensor E_{ij} is constructed as

$$E_{ij} = (1 - \nu) \delta_{ij} + \nu (-P_{ij}/p), \tag{5}$$

where δ_{ij} is the Kronecker delta, $P_{ij}(t, \boldsymbol{x})$ denotes the local stress tensor, $p(t, \boldsymbol{x}) = -P_{kk}/3$ is the local gas pressure, and ν is a model parameter linked with the gas Prandtl number. To guarantee the positive semi-definiteness of the diffusion coefficient in Eq. (4), ν is defined as

$$\nu = \max \left\{ 1 - \frac{3}{2 \, \text{Pr}}, \ \frac{1}{1 - \lambda_{\max}} \right\}, \tag{6}$$

where Pr is the correct value of the gas Prandtl number (e.g., Pr = 2/3 for monatomic gases) and $\lambda_{\max}$ is the maximum eigenvalue of the normalized stress tensor $(-P_{ij}/p)$. Based on this ν, the local relaxation time $\tau(t, \boldsymbol{x})$ is defined as

$$\tau(t, \boldsymbol{x}) = 2(1 - \nu) \frac{\mu(T(t, \boldsymbol{x}))}{p(t, \boldsymbol{x})}, \tag{7}$$

where the gas viscosity $\mu(T)$ is a known function of temperature $T(t, \boldsymbol{x})$, and the expression of $\mu(T)$ is provided by gas-kinetic theory using a model of the collision cross section of the gas molecule.

As shown above, the coefficients in the ES-FP operator involve many macroscopic flow properties, which should be regarded as the statistical moments of the velocity distribution function $f(t, \boldsymbol{x}, \boldsymbol{c})$.

The formulas for number density n, gas velocity $\boldsymbol{u}$, stress tensor $\boldsymbol{P}$, and temperature T are

$$n(t,\boldsymbol{x}) = \int_{\mathbb{R}^3} f(t,\boldsymbol{x},\boldsymbol{c})\mathrm{d}\boldsymbol{c}, \tag{8}$$

$$u_i(t,\boldsymbol{x}) = \frac{\int_{\mathbb{R}^3} c_i f(t,\boldsymbol{x},\boldsymbol{c})\,\mathrm{d}\boldsymbol{c}}{n(t,\boldsymbol{x})}, \tag{9}$$

$$P_{ij}(t,\boldsymbol{x}) = -\int_{\mathbb{R}^3} mC_iC_j f(t,\boldsymbol{x},\boldsymbol{c})\,\mathrm{d}\boldsymbol{c}, \tag{10}$$

$$T(t,\boldsymbol{x}) = \frac{\int_{\mathbb{R}^3} \left(\frac{1}{2}mC^2\right) f(t,\boldsymbol{x},\boldsymbol{c})\,\mathrm{d}\boldsymbol{c}}{\frac{3}{2}k_{\mathrm{B}}n(t,\boldsymbol{x})}, \tag{11}$$

where $\boldsymbol{C}$ denotes the thermal velocity of a molecule, and it is defined as $\boldsymbol{C} = \boldsymbol{c} - \boldsymbol{u}$.

The ES-FP model preserves the essential properties of the full Boltzmann equation and meets the basic requirements for a proper gas-kinetic model.[66] Specifically, it can be proved that (1) a gas system governed by the ES-FP model obeys the laws of conservation of mass, momentum, and energy, as well as the second law of thermodynamics (H-theorem); (2) in the limits of Kn $\to \infty$ and Kn $\to 0$, the ES-FP model yields the free-molecular and the equilibrium solutions, respectively, which are identical to those derived from the Boltzmann equation; and (3) in the continuum regime (Kn $\ll 1$), applying the first-order Chapman–Enskog analysis[78] to the ES-FP equation will recover the Navier–Stokes equations of compressible viscous flows.

The conservative property of the ES-FP model, which is the topic of interest in this paper, means that the hydrodynamic conservation laws

$$\frac{\partial}{\partial t}\begin{pmatrix}\rho\\ \rho u_j\\ \rho e\end{pmatrix} + \frac{\partial}{\partial x_i}\begin{pmatrix}\rho u_i\\ \rho u_j u_i + p\delta_{ij} - \pi_{ij}\\ \rho e u_i + p u_i - \pi_{ij}u_j + q_i\end{pmatrix} = \boldsymbol{0} \tag{12}$$

can be obtained by taking moments of Eq. (4). In Eq. (12), ρ denotes the mass density, e denotes the total energy per unit mass, π_{ij} is the viscous stress tensor, and q_i is the heat flux vector. In fact, these conservation laws are direct results of the following property of the ES-FP operator:

$$\int_{\mathbb{R}^3}\begin{pmatrix}m\\ mc_j\\ mc^2/2\end{pmatrix} S_{\mathrm{FP}}^{\mathrm{ES}}(f)\,\mathrm{d}\boldsymbol{c} = \boldsymbol{0}, \tag{13}$$

indicating that mass, momentum, and energy are conserved during molecular interactions. Theoretically, Eq. (13) is guaranteed, owing to the construction of $S_{\mathrm{FP}}^{\mathrm{ES}}(f)$ together with the relations between macroscopic quantities and the distribution function f [see Eqs. (8)–(11)]. However, in a numerical implementation of the ES-FP model, special care may be needed to satisfy the conservation conditions described by Eq. (13).

B. Langevin dynamics corresponding to ES-FP model

Instead of a direct discretization of Eq. (4), the ES-FP model is numerically simulated with stochastic particle-based algorithms in this paper. For this purpose, the dynamical law of the individual behavior of gas molecules is required. Fortunately, theories of continuous stochastic processes and stochastic differential equations (SDEs) show that a Fokker–Planck-type equation for the distribution function f $(t, \boldsymbol{x}, \boldsymbol{c})$ is equivalent to its corresponding SDEs for molecular state $\{\boldsymbol{x}(t), \boldsymbol{c}(t)\}$, called the Langevin equations.[79,80]

The ES-FP equation (4) can be derived if the motion of each gas molecule follows the Langevin equations

$$\frac{\mathrm{d}x_i}{\mathrm{d}t} = c_i, \tag{14}$$

$$\frac{\mathrm{d}c_i}{\mathrm{d}t} = -\frac{1}{\tau}(c_i - u_i) + \sqrt{\frac{2k_{\mathrm{B}}T}{m\tau}}L_{ij}\dot{W}_j(t), \tag{15}$$

where $\boldsymbol{W}(t)$ denotes the 3D standard Wiener process, and its time derivative has the properties of white noise,

$$\left\langle \dot{W}_i(t)\right\rangle = 0, \quad \left\langle \dot{W}_i(t)\dot{W}_j(t')\right\rangle = \delta_{ij}\delta(t-t'). \tag{16}$$

In Eq. (15), $\boldsymbol{L}$ is a dimensionless matrix associated with the tensor $\boldsymbol{E}$ defined by Eq. (5), and the relation between $\boldsymbol{L}$ and $\boldsymbol{E}$ is

$$L_{ik}L_{jk} = E_{ij}. \tag{17}$$

For numerical convenience, matrix $\boldsymbol{L}$ can be taken as the Cholesky factor of $\boldsymbol{E}$. It can be mathematically proved that the above Langevin dynamics and the ES-FP equation (4) describe the same stochastic process of $\{\boldsymbol{x}(t), \boldsymbol{c}(t)\}$.[79,80]

From a physical point of view, Eqs. (14)–(17) provide a coarse-grained model of the molecular dynamics, by exerting a drag force and a rapidly fluctuating random force on each gas molecule to effectively replace the real molecular interactions. The linear drag force and the anisotropic fluctuating force in Eq. (15) correspond to the drift term and the diffusion term in the ES-FP equation (4), respectively. In Secs. III and IV, the key step of a particle ES-FP scheme is to evolve each particle by integrating the Langevin equations (14) and (15).

C. Initial and boundary conditions

Similar to any gas-kinetic description of flow problems, the ES-FP model requires initial and boundary conditions for the distribution of molecular velocities. In this paper, the initial flow field is uniform and is in thermal equilibrium, and therefore the initial molecular velocities are sampled from a Maxwellian distribution under macroscopic parameters n_{ini}, $\boldsymbol{u}_{\mathrm{ini}}$, and T_{ini}. At freestream boundaries, the velocity distribution is a Maxwellian distribution under freestream parameters n_∞, $\boldsymbol{u}_\infty$, and T_∞. Wall surfaces are stationary and isothermal at temperature T_{w}. For gas–surface interactions, the diffuse reflection model with full thermal accommodation is assumed. At a plane of symmetry, the molecular velocities are specularly reflected.

III. REVIEW OF PARTICLE ES-FP SCHEME

This section briefly reviews the particle-based ES-FP scheme proposed in Ref. 66. This scheme closely follows the methodology of Jenny *et al.*,[32] which is characterized by the coupling of free-molecular moves and intermolecular collisions over one time

step. In this section, a specially designed integration technique for stochastic differential equations (14) and (15) is introduced at first, and then the algorithm of this particle ES-FP scheme is outlined.

A. Stochastic integration

Assume that the local macroscopic quantities $\boldsymbol{u}$, T, τ, and $\boldsymbol{L}$ in the Langevin equations are known and frozen over the time interval $[t, t + \Delta t]$. A statistically exact integration scheme for the Langevin equations (14) and (15) can be written as[66]

$$x_i(t+\Delta t) = x_i(t) + u_i\Delta t + [c_i(t) - u_i](1 - e^{-\Delta t/\tau})\tau + \sqrt{B_{xx}}L_{ik}\xi_k, \quad (18)$$

$$c_i(t + \Delta t) = u_i + [c_i(t) - u_i]e^{-\Delta t/\tau} + \sqrt{B_{cx}{}^2/B_{xx}}L_{ik}\xi_k + \sqrt{B_{cc} - (B_{cx}{}^2/B_{xx})}L_{ik}\eta_k, \quad (19)$$

where $\boldsymbol{\xi}$ and $\boldsymbol{\eta}$ are two independent 3D random vectors that obey the standard normal distribution so that

$$\langle\xi_i\rangle = 0,\ \langle\eta_i\rangle = 0,\ \langle\xi_i\xi_j\rangle = \delta_{ij},\ \langle\eta_i\eta_j\rangle = \delta_{ij},\ \langle\xi_i\eta_j\rangle = 0. \quad (20)$$

Besides, the coefficients B_{xx}, B_{cx}, and B_{cc} are

$$B_{xx} = \tau^2(k_B T/m)\left(-3 + 2\Delta t/\tau + 4e^{-\Delta t/\tau} - e^{-2\Delta t/\tau}\right), \quad (21)$$

$$B_{cx} = \tau(k_B T/m)\left(1 - e^{-\Delta t/\tau}\right)^2, \quad (22)$$

$$B_{cc} = (k_B T/m)\left(1 - e^{-2\Delta t/\tau}\right). \quad (23)$$

On condition that $\boldsymbol{c}(t)$ is known, the statistical moments of the displacement $\Delta\boldsymbol{x} = \boldsymbol{x}(t + \Delta t) - \boldsymbol{x}(t)$ and the velocity increment $\Delta\boldsymbol{c} = \boldsymbol{c}(t + \Delta t) - \boldsymbol{c}(t)$ can be obtained from Eqs. (18)–(23) and then compared with the theoretical expressions derived from the Langevin equations (14) and (15). The comparison shows that the integration formulas Eqs. (18) and (19) exactly preserve the theoretical expressions of the first-order and second-order moments of $\Delta\boldsymbol{x}$ and $\Delta\boldsymbol{c}$:

$$\langle\Delta x_i\rangle = u_i\Delta t + [c_i(t) - u_i]\left(1 - e^{-\Delta t/\tau}\right)\tau, \quad (24)$$

$$\langle\Delta c_i\rangle = [c_i(t) - u_i]\left(e^{-\Delta t/\tau} - 1\right), \quad (25)$$

$$\langle\Delta x_i\Delta x_j\rangle - \langle\Delta x_i\rangle\langle\Delta x_j\rangle = \tau^2(k_B T/m) \times \left(-3 + 2\Delta t/\tau + 4e^{-\Delta t/\tau} - e^{-2\Delta t/\tau}\right)E_{ij}, \quad (26)$$

$$\langle\Delta c_i\Delta c_j\rangle - \langle\Delta c_i\rangle\langle\Delta c_j\rangle = (k_B T/m)\left(1 - e^{-2\Delta t/\tau}\right)E_{ij}, \quad (27)$$

$$\langle\Delta c_i\Delta x_j\rangle - \langle\Delta c_i\rangle\langle\Delta x_j\rangle = \tau(k_B T/m)\left(1 - e^{-\Delta t/\tau}\right)^2 E_{ij}. \quad (28)$$

B. Outline of algorithm

The particle ES-FP scheme shares the framework of the standard DSMC method. A computational grid with boundary settings should be prepared before the simulation begins. Each computational particle represents a large number of real molecules and evolves according to the Langevin dynamics and boundary conditions described in Sec. II. The particle ES-FP algorithm in Ref. 66 is briefly described in Algorithm 1.

ALGORITHM 1. Outline of the stochastic particle algorithm in Ref. 66 for the ES-FP gas-kinetic model.

1. Initialization

Initialize the macroscopic flow field and assign to each grid cell a proper number of computational particles with random positions $\boldsymbol{x}(0)$ and random velocities $\boldsymbol{c}(0)$.

2. Particle evolution

In a loop over all computational particles:

- Find the particle position $\boldsymbol{x}(t)$ at time t. Local macroscopic parameters $\boldsymbol{u}(t, \boldsymbol{x}(t))$, $T(t, \boldsymbol{x}(t))$, $\boldsymbol{L}(t, \boldsymbol{x}(t))$, and $\tau(t, \boldsymbol{x}(t))$ will be used in the integration formulas [Eqs. (18) and (19)] for the particle.
- Generate independent standard normal random vectors $\boldsymbol{\xi}$ and $\boldsymbol{\eta}$ for the particle.
- Update the particle position and velocity using Eqs. (18) and (19). Meanwhile, the particle is being tracked. When the particle hits a boundary element, the corresponding boundary treatment will be performed.

3. Statistical procedure

In a loop over all grid cells:

- Calculate the macroscopic flow properties by averaging molecular properties over the particles located in this cell.
- For steady flow problems, an exponentially weighted time averaging strategy[32] is used to reduce the statistical noise in the macroscopic flow field.
- Determine the parameter ν [Eq. (6)], the tensor $\boldsymbol{E}$ [Eq. (5)], the Cholesky decomposition matrix $\boldsymbol{L}$ of $\boldsymbol{E}$ [Eq. (17)], and the relaxation time τ [Eq. (7)].

Advance the physical time to $t + \Delta t$. If the required number of time steps is reached, go to step 4. Otherwise, go to step 2.

4. Output

Output the results of macroscopic flow field and the distributions of pressure, friction, and heat flux along the wall surface.

IV. CONSERVATIVE PARTICLE ES-FP SCHEME

The numerical performance of the scheme described in Sec. III has been assessed in Ref. 66. In this ES-FP scheme, due to the strong coupling of free-molecular moves and intermolecular collisions, it is difficult to analyze whether this scheme can numerically ensure the conservation of momentum and energy or not. Toward a truly conservative particle ES-FP scheme, this section begins with the decoupling of free-molecular moves and intermolecular collisions. On this basis, the numerical implementation of a conservative particle ES-FP scheme is described.

A. Approximation of the exact stochastic integral solution

Consider the approximation of the position update formula [Eq. (18)] in the limit of the vanishing time step Δt. The Taylor expansion of Eqs. (18) and (21) with respect to $(\Delta t/\tau)$ leads to

$$x_i(t+\Delta t) = \underbrace{x_i(t) + u_i\Delta t + \tau[c_i(t)-u_i]\left[\frac{\Delta t}{\tau} + O\left(\frac{\Delta t}{\tau}\right)^2\right]}_{\text{deterministic terms}} + \underbrace{\sqrt{\tau^2\frac{k_BT}{m}\left[\frac{2}{3}\left(\frac{\Delta t}{\tau}\right)^3 + O\left(\frac{\Delta t}{\tau}\right)^4\right]}L_{ik}\xi_k}_{\text{random term}}, \quad \frac{\Delta t}{\tau} \to 0, \tag{29}$$

where the random term is $O((\Delta t/\tau)^{3/2})$. By neglecting terms of 3/2 order and higher, the position update formula is reduced to the free-flight formula

$$x_i(t+\Delta t) = x_i(t) + c_i(t)\Delta t. \tag{30}$$

Since Eq. (30) is deterministic, there is no need to preserve the covariance of $\Delta\boldsymbol{c}$ and $\Delta\boldsymbol{x}$ [Eq. (28)], and thus, the two random terms in Eq. (19) can be replaced by a sole random term. The reduced formula to update molecular velocity becomes

$$c_i(t+\Delta t) = u_i + [c_i(t)-u_i]e^{-\Delta t/\tau} + \sqrt{(k_BT/m)(1-e^{-2\Delta t/\tau})}L_{ik}\xi_k, \tag{31}$$

where $\boldsymbol{\xi}$ is a 3D random vector that obeys the standard normal distribution and, therefore,

$$\langle\xi_i\rangle = 0, \ \langle\xi_i\xi_j\rangle = \delta_{ij}. \tag{32}$$

Equation (31) is actually the solution of the Langevin equation (15), preserving the exact expressions of $\langle\Delta c_i\rangle$ and $\langle\Delta c_i\Delta c_j\rangle$ [Eqs. (25) and (27)]. Note that the random term in Eq. (31) can never be neglected when $(\Delta t/\tau)$ approaches 0 because this random term is a semi-order infinitesimal $O((\Delta t/\tau)^{1/2})$.

Equations (30) and (31) describe the simplified ES-FP particle evolution under the condition of a small time step. Such a simplification implies the decoupling of free-molecular moves and intermolecular collisions. Therefore, a time-splitting strategy can be used in the implementation of the particle ES-FP method. In each time step, the ES-FP equation is split into a free-molecular kinetic equation,

$$\frac{\partial f}{\partial t} = -c_i\frac{\partial f}{\partial x_i}, \tag{33}$$

and an equation for the molecular velocity evolution due to intermolecular collisions,

$$\frac{\partial f}{\partial t} = \frac{1}{\tau}\frac{\partial}{\partial c_i}[(c_i-u_i)f] + \left(\frac{k_BT}{m\tau}\right)E_{ij}\frac{\partial^2 f}{\partial c_i\partial c_j}. \tag{34}$$

Accordingly, the particle evolution is implemented in two sequential stages. First, following Eq. (30), all particles move at constant velocities along the straight lines that are actually the characteristic lines of Eq. (33). Then, all particle positions are fixed, and all particles are indexed to the computational cells. In a loop over all cells, one can determine the cell values of macroscopic parameters ($\boldsymbol{u}$, T, $\boldsymbol{L}$, and τ) and update the velocity of each particle located in the cell using Eq. (31), which precisely corresponds to the analytical solution of Eq. (34). As a consequence of using the decoupled scheme with Eqs. (30) and (31), the time step Δt of particle simulation has to be a fraction of the molecular collision time scale.

B. Conditions for the conservation of momentum and energy

Upon the decoupling of free-molecular moves and intermolecular collisions, the conservative property of a particle scheme can be analyzed. Clearly, the particle move procedure [Eq. (30)] is conservative. This is because particles are the carriers of mass, momentum, and energy in the simulation, and these properties of each particle (m, $m\boldsymbol{c}$, and $mc^2/2$) remain unchanged during the free-molecular moves. Therefore, the present decoupled scheme will be conservative as long as the velocity evolution procedure follows the physical fact that mass, momentum, and energy are conserved in intermolecular collisions, which is already stated by the important property [Eq. (13)] of the ES-FP operator.

In the decoupled scheme, the particle velocity evolution can be implemented cell by cell. In this process, there is no flux through cell faces because particles do not move at this stage. Thus, the mass, momentum, and energy in each cell should be the same before and after the velocity evolution. For mass, this requirement is met obviously. For momentum and energy, it means the velocity update formula [Eq. (31)] is supposed to ensure

$$\sum_{\text{pic}}[mc_i(t+\Delta t)] = \sum_{\text{pic}}[mc_i(t)], \tag{35}$$

$$\sum_{\text{pic}}\left[\frac{1}{2}mc^2(t+\Delta t)\right] = \sum_{\text{pic}}\left[\frac{1}{2}mc^2(t)\right], \tag{36}$$

where $\sum_{\text{pic}}(\cdot)$ represents the summation over particles in the cell.

Although Eq. (31) is the statistically exact solution of the Langevin equation (15) [or equivalently the split ES-FP equation (34)], it may not ensure Eqs. (35) and (36) due to the details in the numerical implementation. Consider a computational cell that contains N particles. As shown by Eq. (31), the evolution of each particle velocity $\boldsymbol{c}(t)$ is driven by a normal random vector $\boldsymbol{\xi}$, and therefore, a set of normal random vectors $\{\boldsymbol{\xi}^{(1)}, \boldsymbol{\xi}^{(2)}, \ldots, \boldsymbol{\xi}^{(N)}\}$ need to be generated for this cell. Here, we propose the following sufficient conditions to satisfy Eqs. (35) and (36).

Condition 1. The macroscopic flow velocity $\boldsymbol{u}$ and temperature T in Eq. (31) should be derived from the microscopic information of the N particles located within this cell at the instant just before performing the velocity evolution procedure. To be specific, the definitions of $\boldsymbol{u}$ and T should be

$$\left(\sum_{\text{pic}} m\right) u_i = \sum_{\text{pic}} [mc_i(t)], \tag{37}$$

$$\frac{1}{2}\left(\sum_{\text{pic}} m\right) u^2 + N\left(\frac{3}{2}k_{\text{B}}T\right) = \sum_{\text{pic}} \left[\frac{1}{2}mc^2(t)\right]. \tag{38}$$

The above equations emphasize on the instantaneous correspondence between the macroscopic quantities and the molecular velocity distribution in the ES-FP kinetic model [see Eqs. (8)–(11)].

Condition 2. The set of normal random vectors $\{\boldsymbol{\xi}^{(1)}, \boldsymbol{\xi}^{(2)}, \ldots, \boldsymbol{\xi}^{(N)}\}$ satisfy

$$\sum_{n=1}^{N} \xi_i^{(n)} = 0, \tag{39}$$

$$\sum_{n=1}^{N} \xi_i^{(n)} \xi_j^{(n)} = N\delta_{ij}. \tag{40}$$

Although there are many mature techniques to sample each $\boldsymbol{\xi}^{(n)}$ from the standard normal distribution, Eqs. (39) and (40) impose a much stronger constraint on $\{\boldsymbol{\xi}^{(1)}, \boldsymbol{\xi}^{(2)}, \ldots, \boldsymbol{\xi}^{(N)}\}$ than the theoretical expectations of $\boldsymbol{\xi}$, as shown in Eq. (32).

The Appendix shows that these conditions ensure the conservation of momentum and energy. In practice, condition 1 can be satisfied as long as an instantaneous averaging strategy is used when calculating the macroscopic quantities involved in Eq. (31). However, condition 2 is inevitably violated, unless the number of particles N approaches infinity.

C. Conservative particle scheme

One can circumvent condition 2 in Sec. IV B and still enforce the conservation of momentum and energy, by adding a velocity correction procedure after evolving the particle velocities according to the Langevin dynamics. In this way, the conservative property of the scheme can get rid of the reliance on the statistical characteristics of random variables.

By replacing $\boldsymbol{c}(t + \Delta t)$ with a temporary variable $\tilde{\boldsymbol{c}}$, Eq. (31) can be rewritten as

$$\tilde{c}_i = u_i + [c_i(t) - u_i]e^{-\Delta t/\tau} + \sqrt{(k_{\text{B}}T/m)(1 - e^{-2\Delta t/\tau})}L_{ik}\xi_k, \tag{41}$$

where the macroscopic flow velocity $\boldsymbol{u}$ and temperature T are defined by Eqs. (37) and (38). Then, based on these temporary molecular velocities $\tilde{\boldsymbol{c}}$, one can define a temporary macroscopic velocity $\tilde{\boldsymbol{u}}$ and a temporary temperature $\tilde{T}$ for each cell,

$$\left(\sum_{\text{pic}} m\right) \tilde{u}_i = \sum_{\text{pic}} (m\tilde{c}_i), \tag{42}$$

$$\frac{1}{2}\left(\sum_{\text{pic}} m\right) \tilde{u}^2 + N\left(\frac{3}{2}k_{\text{B}}\tilde{T}\right) = \sum_{\text{pic}} \left(\frac{1}{2}m\tilde{c}^2\right). \tag{43}$$

ALGORITHM 2. Outline of the stochastic particle algorithm for the ES-FP gas-kinetic model with enforcement of conservation.

1. Initialization

To each grid cell, assign a proper number of computational particles with random positions $\boldsymbol{x}(0)$ and random velocities $\boldsymbol{c}(0)$.

2. Free-molecular moves

- In a loop over all computational particles, move and track each particle using Eq. (30). Meanwhile, implement the boundary conditions of the flow problem.
- Index the particles to the grid cells.

3. Evolution of molecular velocity

In a loop over all grid cells:

- Perform an instantaneous statistical procedure in preparation for the velocity evolution so that the macroscopic parameters involved in the Langevin dynamics are obtained by sampling the particles in this cell at this instant. For example, see Eqs. (37) and (38).
- For each particle in the cell, generate a standard normal random vector $\boldsymbol{\xi}$ and evolve its velocity using Eq. (41).
- Perform a velocity correction procedure. Calculate $\tilde{\boldsymbol{u}}$ and $\tilde{T}$ for the cell, using Eqs. (42) and (43). For each particle in the cell, correct its velocity using Eq. (44).

4. Statistical procedure for output

Calculate the macroscopic flow properties by averaging the molecular information. Similar to the routine in the DSMC method, an accumulative time averaging strategy is used to reduce the statistical noise in the macroscopic results. These macroscopic results are only for the output purpose, and they will not be used in step 3.

Advance the physical time to $t + \Delta t$. If the required number of time steps is reached, go to step 5. Otherwise, go to step 2.

5. Output

Output the results of the macroscopic flow field and the distributions of pressure, friction, and heat flux along the wall surface.

TABLE I. Parameters in the VHS model for argon gas.

Parameter	Recommended value[17]
Reference temperature T_{ref} (K)	273
Reference diameter d_{ref} (m)	4.17×10^{-10}
Viscosity–temperature index ω	0.81
Molecular mass m (kg)	6.63×10^{-26}

If condition 2 in Sec. IV B holds, it can be shown that $\tilde{\boldsymbol{u}}$ and $\tilde{T}$ are identical to $\boldsymbol{u}$ and T, respectively (see the Appendix). However, in general, $\tilde{\boldsymbol{u}}$ is different from $\boldsymbol{u}$, and $\tilde{T}$ is different from T. Therefore, a scaling–shifting transformation

$$c_i(t+\Delta t) = u_i + \sqrt{\frac{T}{\tilde{T}}}(\tilde{c}_i - \tilde{u}_i) \tag{44}$$

will be performed to finally determine the updated velocity $\boldsymbol{c}(t+\Delta t)$ for each particle in the cell. By using the definition of macroscopic properties $\boldsymbol{u}$, T, $\tilde{\boldsymbol{u}}$, and $\tilde{T}$ [Eqs. (37), (38), (42), and (43)], it is straightforward to show that the velocity correction [Eq. (44)] can lead to the conservation of momentum and energy [Eqs. (35) and (36)].

Based on the above considerations in Secs. IV A–IV C, a conservative particle ES-FP scheme can be implemented with Algorithm 2, where some remarkable differences from Algorithm 1 should be noted. In particular, the purpose of the statistical procedure here is twofold: (1) to obtain the macroscopic parameters

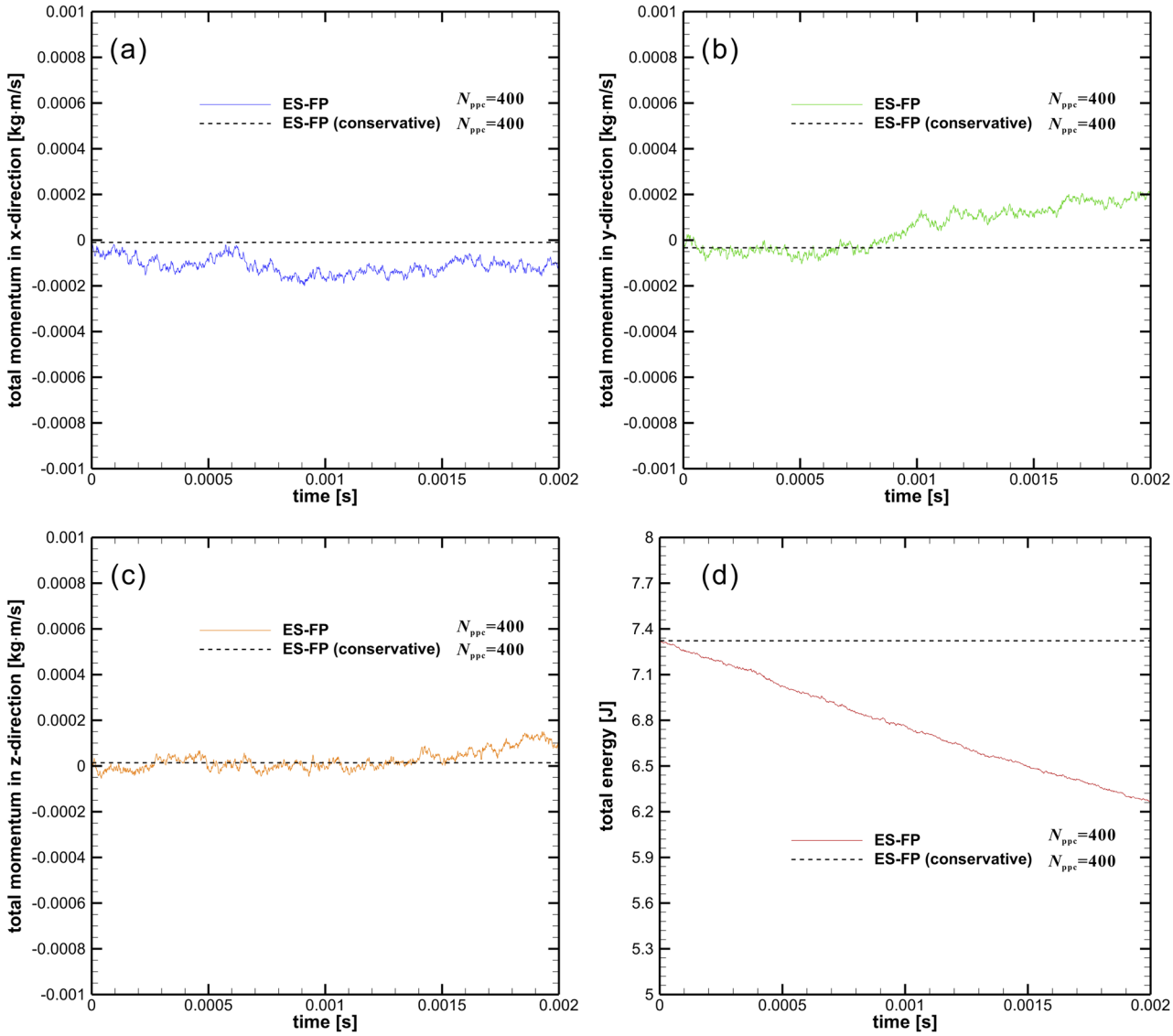

FIG. 1. Time history of the total momentum and the total energy in the entire computational domain: (a) x-component of momentum, (b) y-component of momentum, (c) z-component of momentum, and (d) energy.

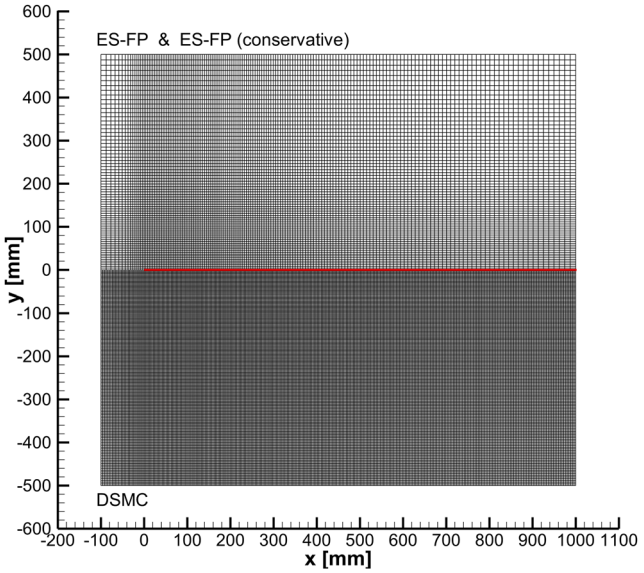

FIG. 2. The computational grids for ES-FP and DSMC simulations of a Mach 6 flow over a flat plate. The thick line stands for the plate.

TABLE II. Freestream and wall conditions of the flat-plate flow.

Parameter	Value
Freestream number density n_∞ (m^{-3})	1.33×10^{20}
Freestream velocity u_∞ (m/s)	1936.07
Freestream temperature T_∞ (K)	300.00
Wall temperature T_w (K)	300.00
Plate length L (m)	1.00
Freestream mean free path λ_∞ (m)	0.01
Freestream mean collision time $\tau_{c,\infty}$ (s)	2.51×10^{-5}
Freestream Mach number M_∞	6.00
Global Knudsen number $\mathrm{Kn}_\infty = \lambda_\infty/L$	0.01

that govern the particle evolution and (2) to output the macroscopic results.[49,50,72] Therefore, two separate statistical modules are suggested in Algorithm 2. The instantaneous averaging strategy is used in step 3 (velocity evolution), while the accumulative time averaging strategy is used in step 4, for the output purpose.

V. NUMERICAL EXAMPLES

In this section, three problems are numerically simulated with two different particle ES-FP schemes described in Sec. III (Algorithm 1) and Sec. IV (Algorithm 2), respectively. Emphasis is placed on the consequences of failing to conserve momentum and energy in the Fokker–Planck-type particle simulations of rarefied gas flows. The DSMC solutions serve as the benchmarks, which are provided by a standard DSMC solver that has been developed and validated in the previous works of the authors.[77,81]

The simulated gas in the following numerical cases is monatomic argon. In the DSMC simulations, the variable hard sphere (VHS) model[16] is assumed for the binary collisions between argon molecules, which leads to the following dependence of gas viscosity on temperature,

$$\mu = \mu_{\mathrm{ref}}\left(\frac{T}{T_{\mathrm{ref}}}\right)^{\omega}, \quad \mu_{\mathrm{ref}} = \frac{15\sqrt{\pi m k_{\mathrm{B}} T_{\mathrm{ref}}}}{2(5-2\omega)(7-2\omega)\pi d_{\mathrm{ref}}^2}. \tag{45}$$

Parameters in the VHS model for argon gas are listed in Table I. In the ES-FP simulations, the Prandtl number Pr = 2/3 and the viscosity–temperature dependence [Eq. (45)] are used as the inputs to the ES-FP model via Eqs. (6) and (7).

A. Homogeneous gas

A spatially homogeneous argon gas is considered. At the initial time, the gas is assumed to be at rest and in thermal equilibrium everywhere, with a number density of 1.294×10^{21} m^{-3} and a temperature of 273 K. A one-dimensional grid is used in the particle simulations to represent a part of the homogeneous gas. The length of the computational domain is 1 m, and both ends of the domain are periodic boundaries. Such a setup implies that the total momentum and the total energy of all gas molecules in the computational domain should stay constant during the system evolution.

Two simulations of this case were performed, using Algorithms 1 and 2, respectively. For both simulations, the 1D computational domain was divided into 2000 equally spaced cells, and each cell contained 400 particles at the initial time. Each particle in the simulations represented about 1.6×10^{15} real molecules. The system was simulated from time $t = 0$ to $t = 2$ ms with a time step of $\Delta t = 1 \times 10^{-6}$ s. At the end of each time step, the total momentum and the total energy of the simulated system were calculated by summing up the molecular properties over the computational domain.

The time history of the total momentum and the total energy in the computational domain is shown in Fig. 1. The results labeled

TABLE III. Computational parameters in the particle simulations of the flat-plate flow.

Parameter	ES-FP or conservative ES-FP	DSMC
Time step (s)	3×10^{-6}	3×10^{-6}
Number of grid cells	165 × 75	330 × 150
Number of particles per cell (initial)	200	50

with "ES-FP" and "ES-FP (conservative)" were obtained by Algorithms 1 and 2, respectively. It is worth noting that the initial molecular velocities were randomly sampled from the Maxwellian distribution with mean velocity $\boldsymbol{u} = \mathbf{0}$ and temperature $T = 273$ K, so the nominal momentum and energy of the simulated gas system at the initial time should be $\mathbf{0}$ and 7.316 J, respectively. However, since the particle number is finite, the initial momentum and energy of the actual system must be slightly different from their nominal values. Whatever the actual initial momentum and energy are, they should be conserved when the system evolves. Therefore, the small discrepancies between the actual and nominal initial conditions can be noticed in Fig. 1 (e.g., the non-zero momentum at $t = 0$), but these discrepancies do not affect the discussion here. While the conservative ES-FP simulation strictly maintains the momentum and energy of the system, the ES-FP simulation without the enforcement of conservation leads to unphysical oscillation and drift of the total momentum, as well as a significant loss in the total energy. For this case, the loss in energy is essentially a drop in gas temperature.

B. Leading edge of flat plate

This subsection is concerned with a supersonic argon gas flow over a zero-thickness flat plate at a zero angle of attack. The 2D computational domain is shown in Fig. 2, where the flat plate is aligned with the x-axis and its leading edge is located at $x = 0$. The plate surface is an isothermal wall, and the diffuse reflection with full thermal accommodation is assumed for the gas–surface interactions. Only half of the flow field needs to be considered, and the symmetric boundary condition is adopted along the x-axis from the flow inlet ($x = -0.1$ m) to the leading edge of plate ($x = 0$). The freestream and wall conditions are listed in Table II.

A comparison was made between the numerical results of two different ES-FP schemes described in Secs. III and IV. The reference results were provided by a standard DSMC simulation. Computational parameters of these particle simulations are listed in Table III, and the computational grids are shown in Fig. 2. Computational parameters and grids in two ES-FP simulations keep consistent with each other. For the DSMC simulation, the selections of computational parameters follow the guidelines required by the DSMC principles. Specifically, the DSMC grid is fine enough to resolve the local mean free path of gas molecules, the DSMC time step size is about one-tenth of the freestream mean collision time, and the initial number of computational particles in a single cell is 50 on average, which satisfies the DSMC requirement by a wide margin.

The computed temperature fields are illustrated in Fig. 3. The results of the ES-FP simulation using Algorithm 1 are compared

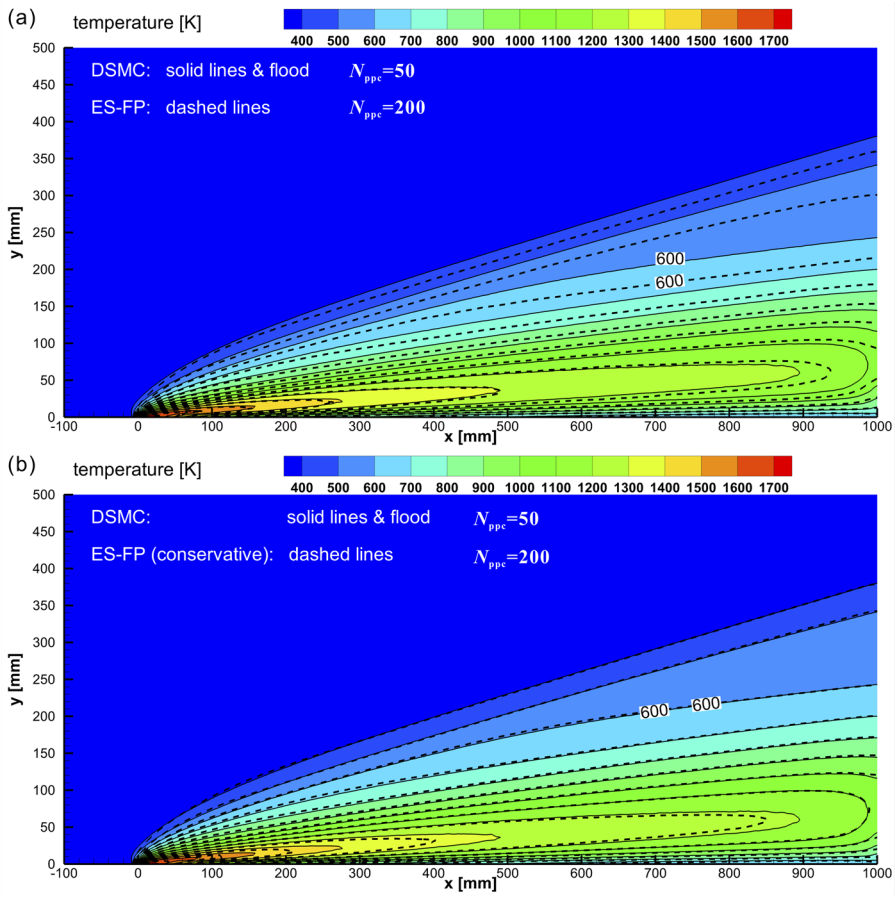

FIG. 3. Temperature contours: (a) ES-FP vs DSMC and (b) conservative ES-FP vs DSMC. The contour lines of $T = 600$ K are labeled. N_{ppc} denotes the average number of computational particles located in one grid cell at the initial time.

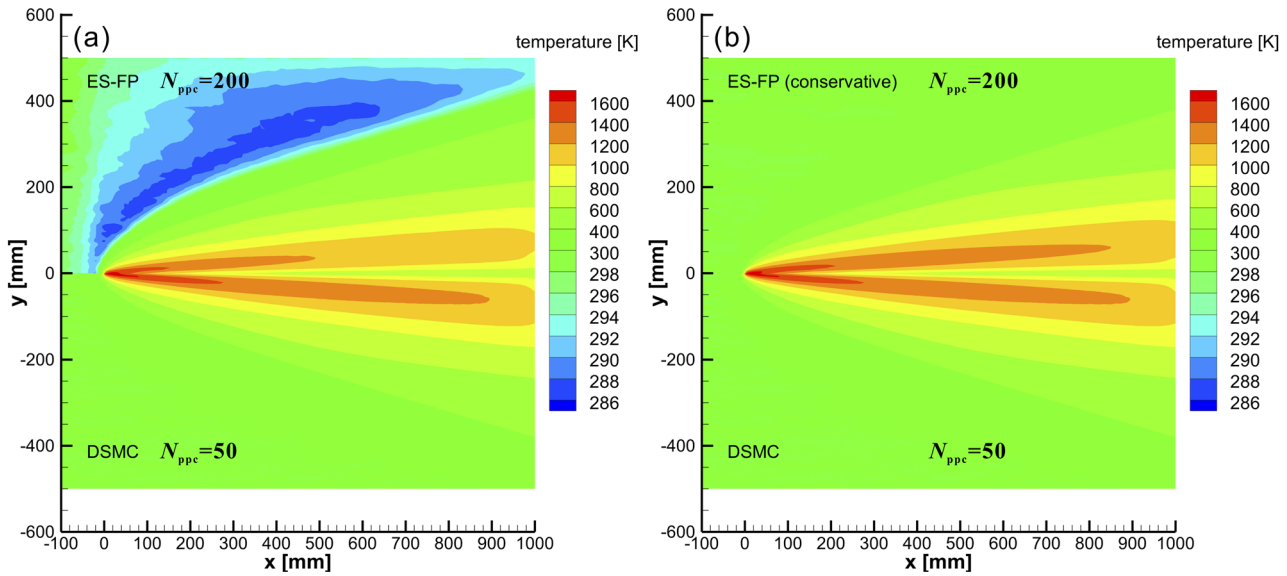

FIG. 4. Anomaly in the temperature field: (a) ES-FP vs DSMC and (b) conservative ES-FP vs DSMC. N_{ppc} denotes the average number of computational particles located in one grid cell at the initial time.

with the DSMC results in Fig. 3(a). Both simulations capture the flow picture that a weak oblique shock wave is generated due to the displacement effect of the boundary layer. However, the shock angle predicted by Algorithm 1 is smaller than the DSMC solution. A close inspection of the contour lines of 600 K can clearly indicate this error. As shown in Fig. 3(b), the conservative ES-FP simulation using Algorithm 2 can achieve better agreement with the DSMC method. If attention is paid to the temperature field in front of the shock wave, which should be undisturbed at the uniform freestream state, one can find that the ES-FP scheme using Algorithm 1 produces an unphysical low-temperature region [Fig. 4(a)]. This anomaly can be effectively

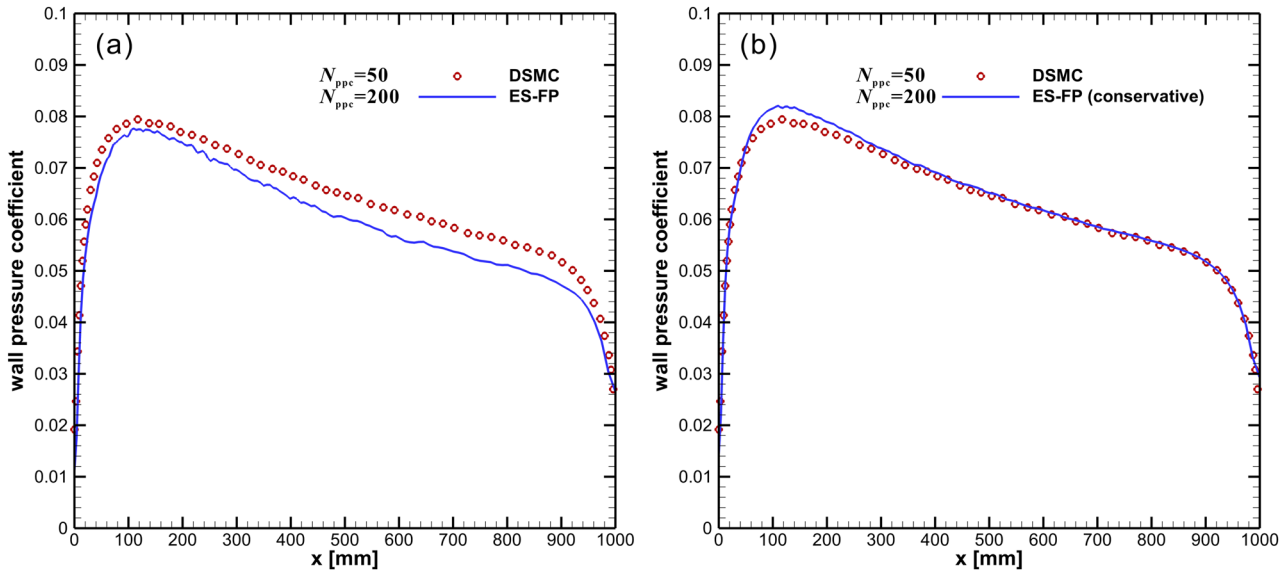

FIG. 5. Distribution of the pressure coefficient along the plate surface: (a) ES-FP vs DSMC and (b) conservative ES-FP vs DSMC. N_{ppc} denotes the average number of computational particles located in one grid cell at the initial time.

removed in the conservative ES-FP simulation using Algorithm 2 [Fig. 4(b)].

Distributions of wall pressure p_w, skin friction τ_w, and wall heat flux q_w along the plate surface are obtained in the particle simulations and plotted in Figs. 5–7, where the dimensionless coefficients of these surface quantities are defined as

$$C_p = (p_w - p_\infty)/\left[(1/2)\rho_\infty u_\infty^2\right], \tag{46}$$

$$C_f = \tau_w/\left[(1/2)\rho_\infty u_\infty^2\right], \tag{47}$$

$$C_h = q_w/\left[(1/2)\rho_\infty u_\infty^3\right]. \tag{48}$$

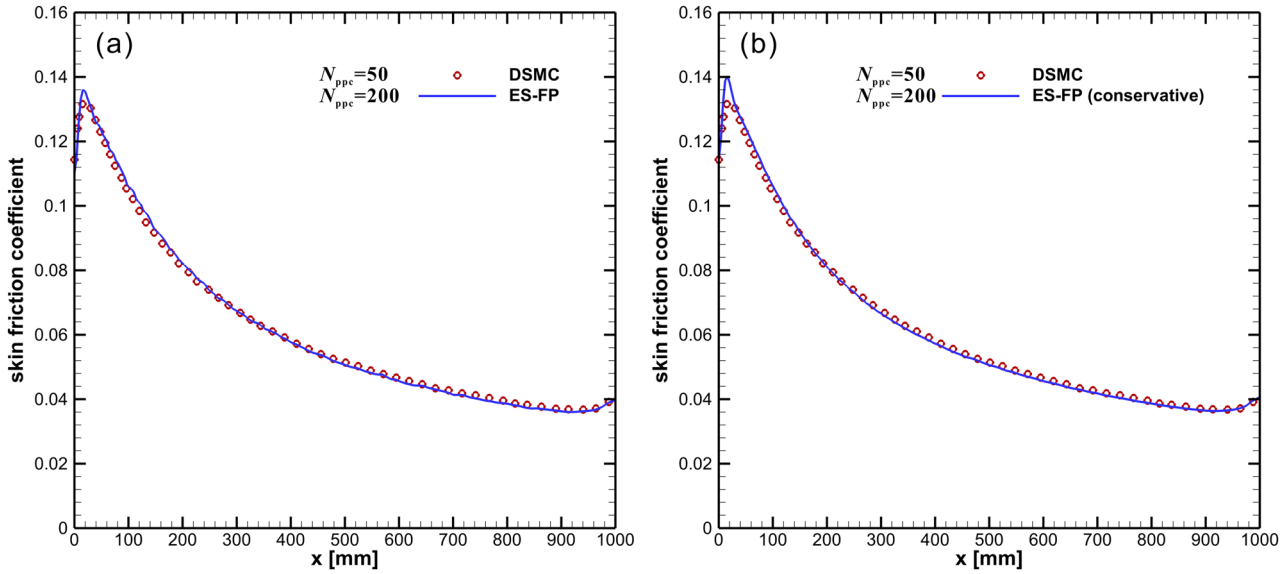

FIG. 6. Distribution of the skin friction coefficient along the plate surface: (a) ES-FP vs DSMC and (b) conservative ES-FP vs DSMC. N_{ppc} denotes the average number of computational particles located in one grid cell at the initial time.

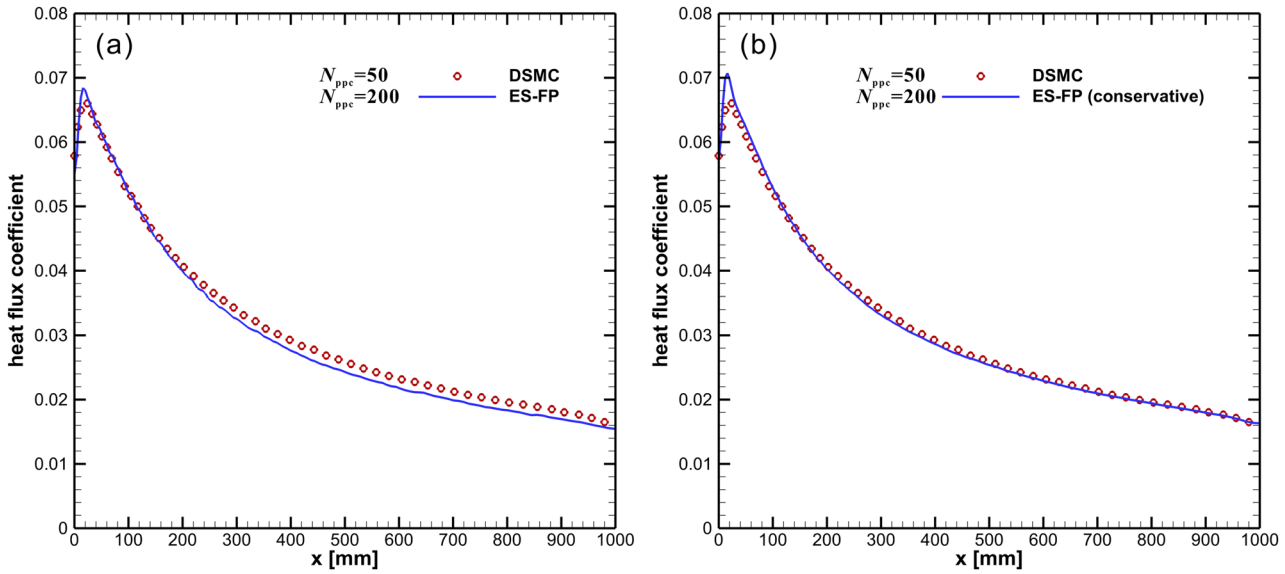

FIG. 7. Distribution of the heat flux coefficient along the plate surface: (a) ES-FP vs DSMC and (b) conservative ES-FP vs DSMC. N_{ppc} denotes the average number of computational particles located in one grid cell at the initial time.

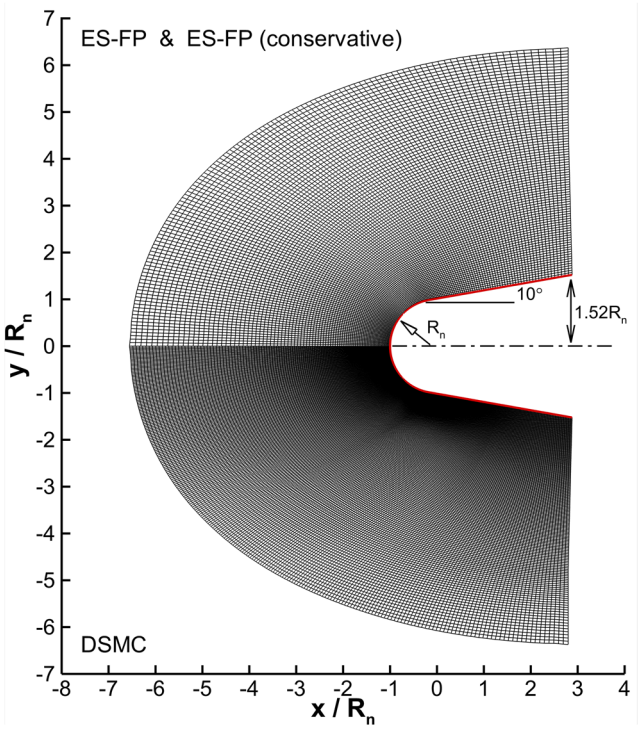

FIG. 8. The computational grids for ES-FP and DSMC simulations of a Mach 6 flow over a blunt body. The thick line stands for the surface of the blunt body.

TABLE IV. Freestream and wall conditions of the blunt-body flow.

Parameter	Value
Freestream number density n_∞ (m^{-3})	1.29×10^{20}
Freestream velocity u_∞ (m/s)	1846.89
Freestream temperature T_∞ (K)	273.00
Wall temperature T_w (K)	273.00
Nose radius R_n (m)	0.10
Freestream mean free path λ_∞ (m)	0.01
Freestream mean collision time $\tau_{c,\infty}$ (s)	2.63×10^{-5}
Freestream Mach number M_∞	6.00
Global Knudsen number $Kn_\infty = \lambda_\infty/R_n$	0.10

Under the condition of $M_\infty = 6$ and $Kn_\infty = 0.01$, this flow problem is characterized by the indirect pressure disturbance due to viscous interaction, the heat transfer due to viscous dissipation, and the strong rarefaction effects in the vicinity of the leading edge. Therefore, it is challenging for numerical simulations to correctly predict all above surface quantities at the same time. For the ES-FP simulation using Algorithm 1, although the skin frictions were predicted accurately, underestimations of wall pressures and wall heat fluxes can be observed, especially for the wall pressures. Remarkable improvements can be achieved by using the conservative ES-FP scheme, as evidenced in Figs. 5(b), 6(b), and 7(b).

C. Blunt body

This subsection is concerned with a supersonic argon gas flow over a 2D round-nosed blunt body at a zero angle of attack. The computational domain is shown in Fig. 8, where the nose radius is denoted by R_n, the half angle is 10°, and the half width of base is $1.52R_n$. The body surface is an isothermal wall, and the diffuse reflection with full thermal accommodation is assumed for the gas–surface interactions. Only half of the flow field needs to be considered, and the symmetric boundary condition is adopted along the x-axis from the flow inlet to the stagnation point. The freestream and wall conditions are listed in Table IV.

A comparison was made between the numerical results of two different ES-FP schemes described in Secs. III and IV. The reference results were provided by a standard DSMC simulation. Computational parameters of these particle simulations are listed in Table V, and the computational grids are shown in Fig. 8. For the DSMC simulation, the time step, the grid resolution, and the number of particles per cell meet the requirements of the DSMC method. For each of the ES-FP schemes, two selections of the number of particles per cell were considered. First, as many as 200 particles per cell were employed. Then, the number of particles per cell was reduced to 50, which is the same as that in the DSMC simulation. The effect of reducing the number of computational particles on the accuracy of two ES-FP schemes will be discussed below.

The steady fields of pressure, velocity, and temperature are presented in Figs. 9–11. In each of these figures, four different ES-FP simulation results are compared with the DSMC results. In the ES-FP simulation using Algorithm 1 and 200 particles per cell, reasonable agreement with the DSMC simulation is obtained in the contours of pressure [Fig. 9(a)], velocity [Fig. 10(a)], and temperature [Fig. 11(a)], except for a little difference in the high pressure region near the stagnation point [Fig. 9(a)]. However, in the ES-FP simulation using Algorithm 1 and 50 particles per cell, the standoff distance of the bow shock wave is obviously underestimated [see Figs. 9(c), 10(c), and 11(c)]. In contrast, the conservative ES-FP scheme using Algorithm 2 demonstrates an insensitivity to the number of employed particles and also shows satisfactory accuracy in comparison with the DSMC method [see subfigures (b) and (d) in Figs. 9–11].

TABLE V. Computational parameters in the particle simulations of the blunt-body flow.

Parameter	ES-FP or conservative ES-FP	DSMC
Time step (s)	1×10^{-6}	1×10^{-6}
Number of grid cells	122 × 88	244 × 176
Number of particles per cell (initial)	200 or 50	50

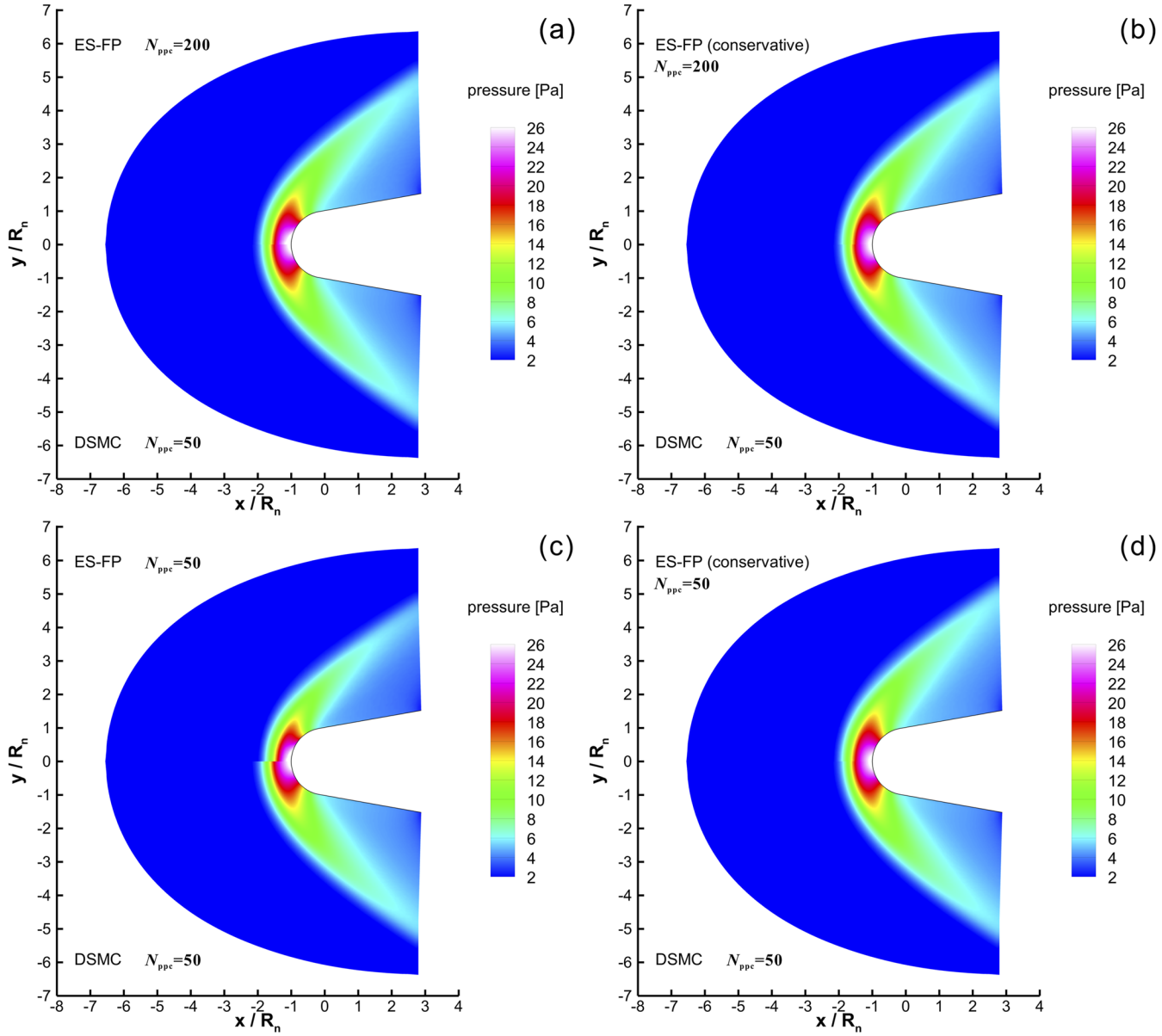

FIG. 9. Pressure contours obtained by different particle ES-FP simulations: (a) ES-FP simulation with N_{ppc} = 200, (b) conservative ES-FP simulation with N_{ppc} = 200, (c) ES-FP simulation with N_{ppc} = 50, and (d) conservative ES-FP simulation with N_{ppc} = 50. The DSMC results serve as the benchmarks. N_{ppc} denotes the average number of computational particles located in one grid cell at the initial time.

Figure 12 gives a closer look at the free stream in front of the shock wave. The anomaly in the computed temperature field, which has been discussed in Sec. V B, is observed again in the ES-FP simulation [Fig. 12(a)] using Algorithm 1, but it is absent in the conservative ES-FP simulation [Fig. 12(b)] using Algorithm 2.

The simulation results of the pressure coefficient, the skin friction coefficient, and the heat flux coefficient along the surface of the blunt body are plotted in Figs. 13–15. For the ES-FP simulation using Algorithm 1, the results are sensitive to the number of particles per cell, and the accuracy becomes worse as the number of particles per cell is reduced. If 200 particles per cell are used, the ES-FP

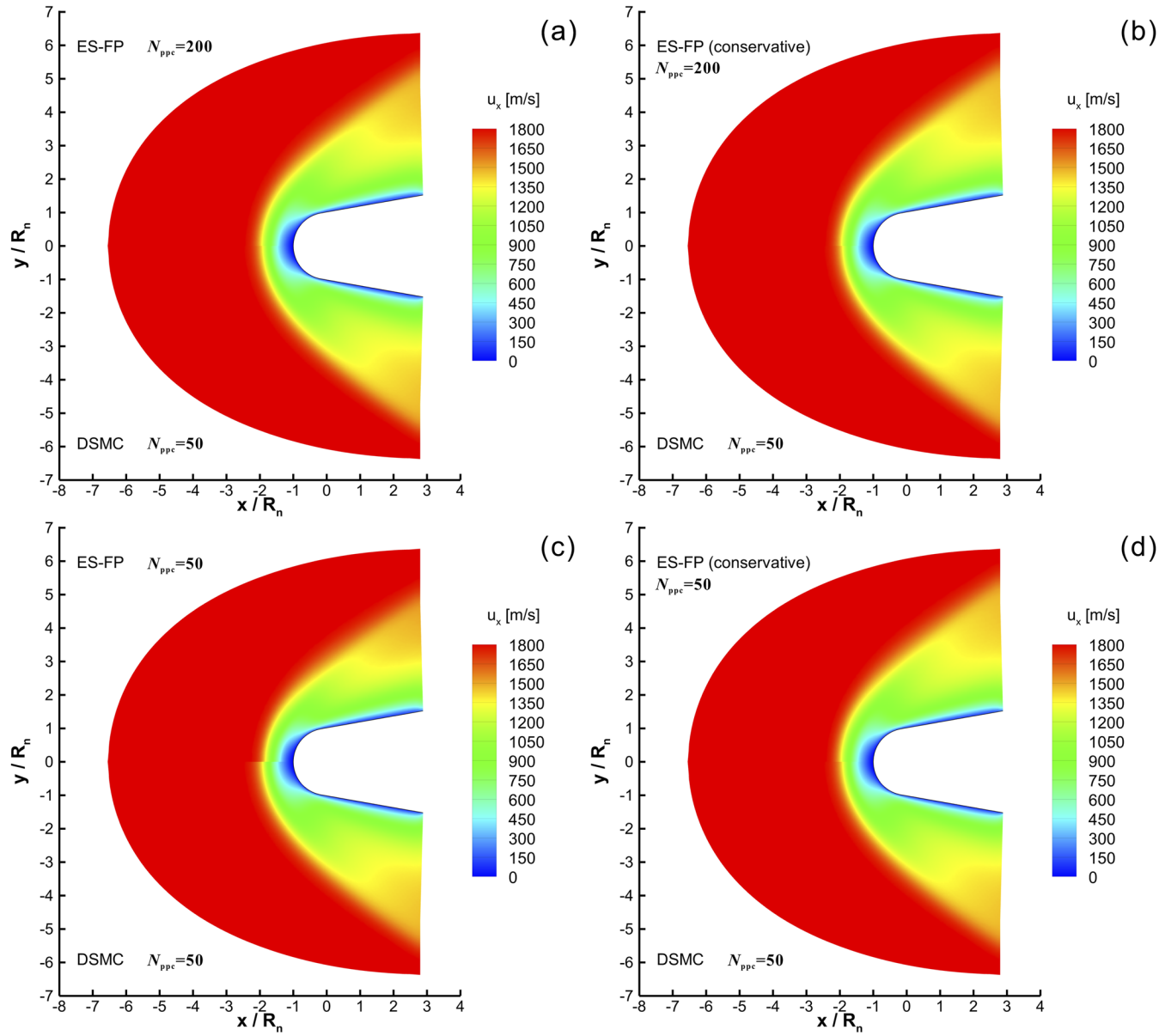

FIG. 10. Contours of the *x*-component of the flow velocity obtained by different particle ES-FP simulations: (a) ES-FP simulation with N_{ppc} = 200, (b) conservative ES-FP simulation with N_{ppc} = 200, (c) ES-FP simulation with N_{ppc} = 50, and (d) conservative ES-FP simulation with N_{ppc} = 50. The DSMC results serve as the benchmarks. N_{ppc} denotes the average number of computational particles located in one grid cell at the initial time.

simulation using Algorithm 1 predicts a higher wall pressure [Fig. 13(a)] and a higher heat flux [Fig. 15(a)] near the stagnation point, and it also overestimates the peak skin friction [Fig. 14(a)]. If 50 particles per cell are used, the ES-FP results of pressure [Fig. 13(c)] and friction [Fig. 14(c)] are higher than the DSMC results on the circular surface but lower than the DSMC results on the flat surface. The largest discrepancy appears in the heat flux distribution [Fig. 15(c)], where the ES-FP results are significantly lower on the whole surface.

As shown in subfigures (b) and (d) in Figs. 13–15, the enforcement of conservation laws substantially improves the accuracy and robustness of the ES-FP simulation. With either N_{ppc} = 200 or

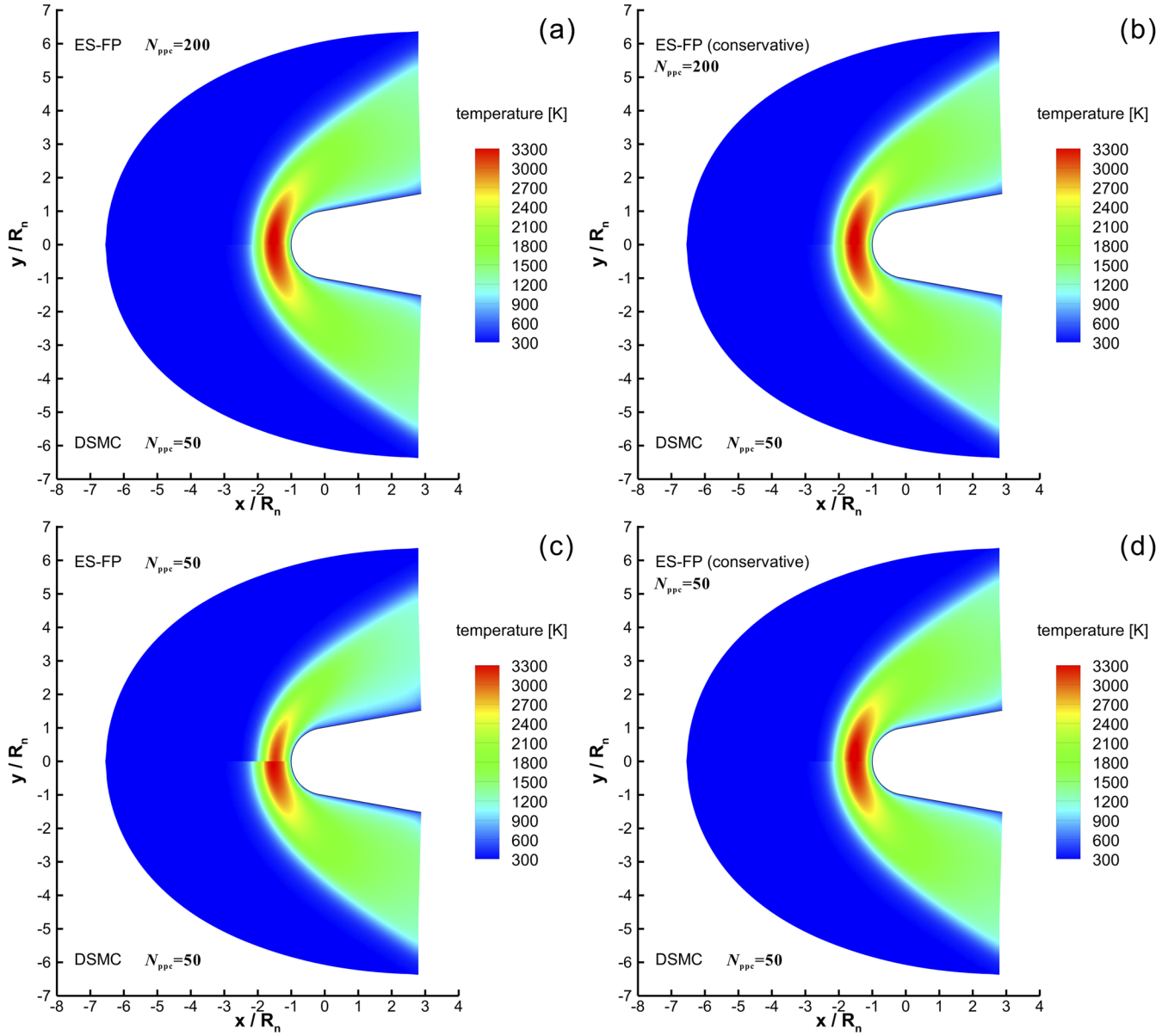

FIG. 11. Temperature contours obtained by different particle ES-FP simulations: (a) ES-FP simulation with N_{ppc} = 200, (b) conservative ES-FP simulation with N_{ppc} = 200, (c) ES-FP simulation with N_{ppc} = 50, and (d) conservative ES-FP simulation with N_{ppc} = 50. The DSMC results serve as the benchmarks. N_{ppc} denotes the average number of computational particles located in one grid cell at the initial time.

N_{ppc} = 50, the surface quantities given by the conservative ES-FP scheme using Algorithm 2 can match well with the DSMC results.

The CPU times were recorded for three of the simulations listed in Table V: the ES-FP simulation with N_{ppc} = 50, the conservative ES-FP simulation with N_{ppc} = 50, and the DSMC simulation. These simulations ended after 40 000 time steps, which simulated the physical process from t = 0 to t = 0.04 s. All computations were performed in serial on a laptop, and the consumed CPU times are 3.1 h for the ES-FP simulation, 3.7 h for the conservative ES-FP simulation, and 7.1 h for the DSMC simulation.

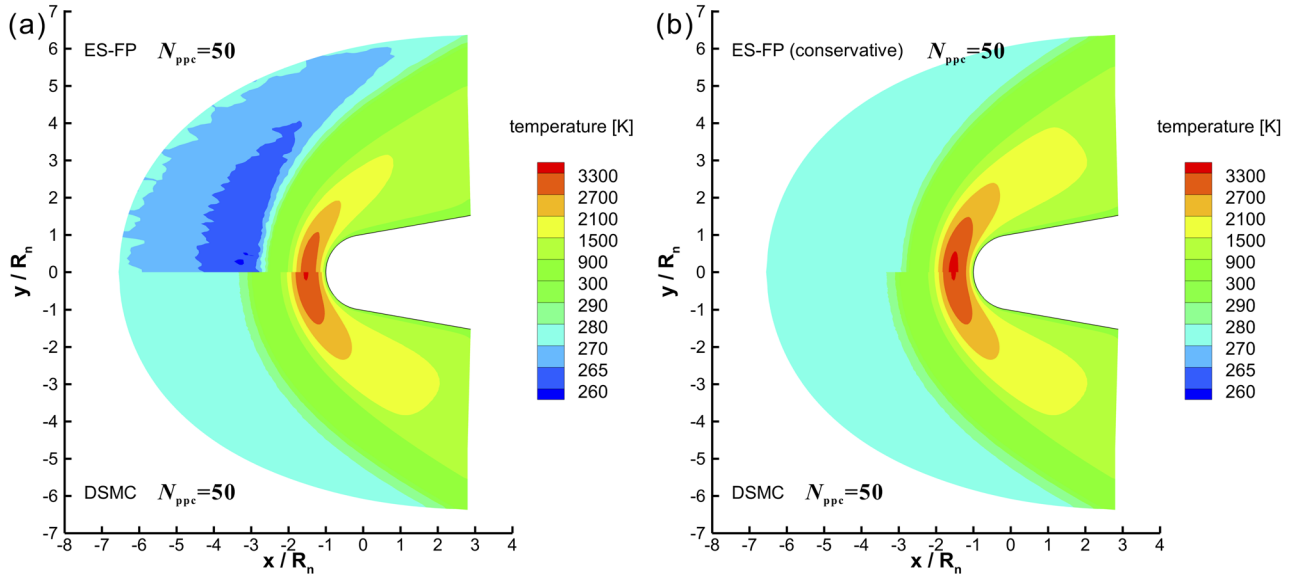

FIG. 12. Anomaly in the temperature field: (a) ES-FP vs DSMC and (b) conservative ES-FP vs DSMC. N_{ppc} denotes the average number of computational particles located in one grid cell at the initial time.

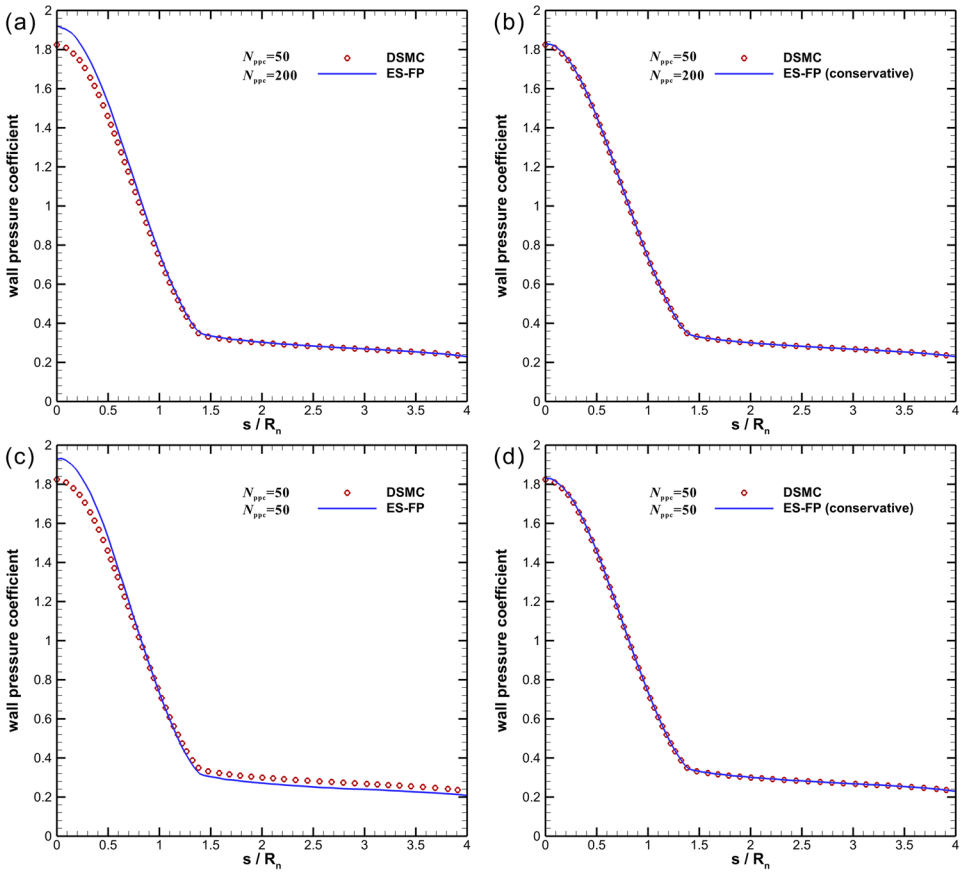

FIG. 13. Distribution of pressure coefficient along the surface of the blunt body: (a) ES-FP simulation with N_{ppc} = 200, (b) conservative ES-FP simulation with N_{ppc} = 200, (c) ES-FP simulation with N_{ppc} = 50, and (d) conservative ES-FP simulation with N_{ppc} = 50. N_{ppc} is the average number of computational particles located in one grid cell at the initial time. The variable *s* is the distance along the surface measured from the leading edge.

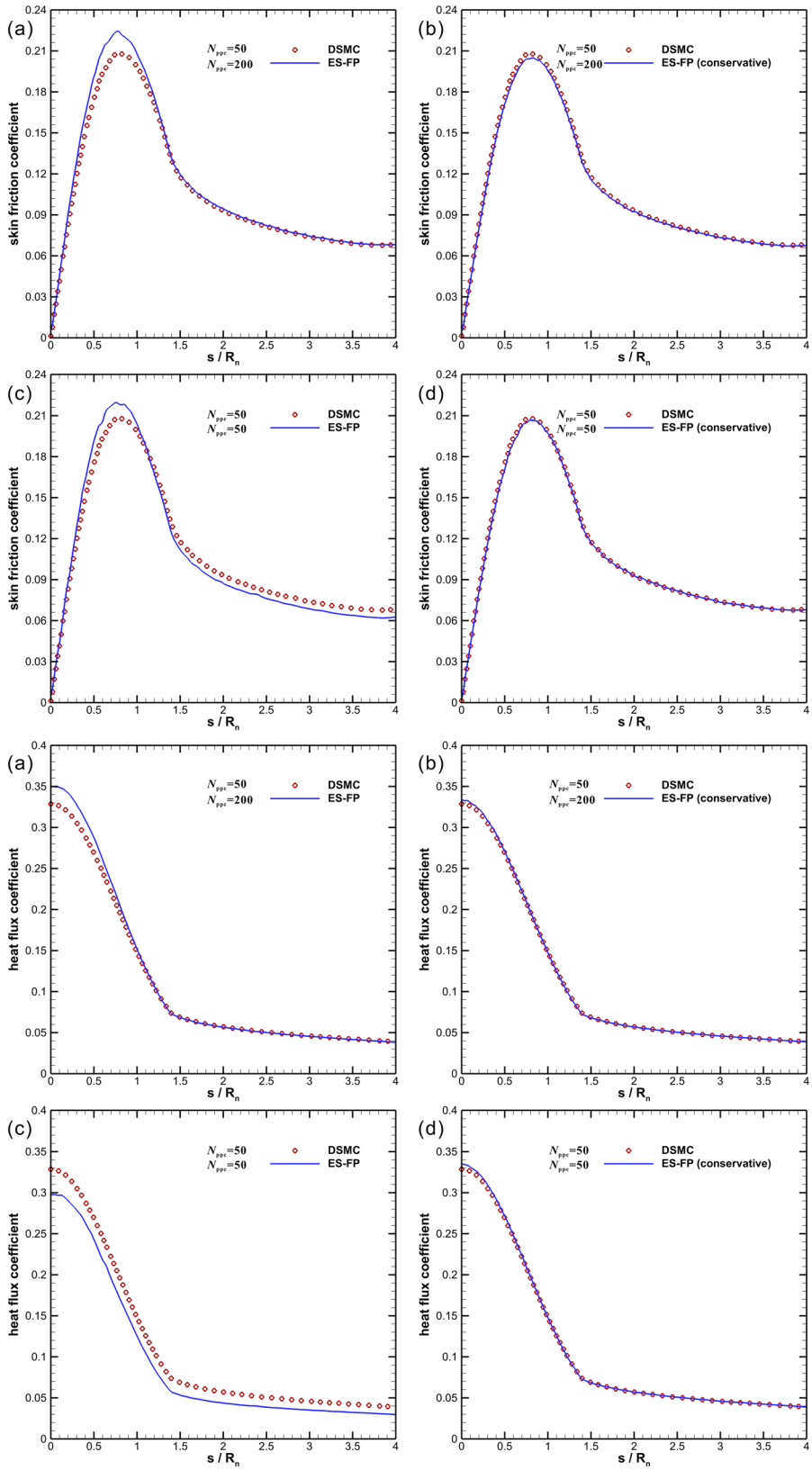

FIG. 14. Distribution of skin friction coefficient along the surface of the blunt body: (a) ES-FP simulation with N_{ppc} = 200, (b) conservative ES-FP simulation with N_{ppc} = 200, (c) ES-FP simulation with N_{ppc} = 50, and (d) conservative ES-FP simulation with N_{ppc} = 50. N_{ppc} is the average number of computational particles located in one grid cell at the initial time. The variable s is the distance along the surface measured from the leading edge.

FIG. 15. Distribution of heat flux coefficient along the surface of the blunt body: (a) ES-FP simulation with N_{ppc} = 200, (b) conservative ES-FP simulation with N_{ppc} = 200, (c) ES-FP simulation with N_{ppc} = 50, and (d) conservative ES-FP simulation with N_{ppc} = 50. N_{ppc} is the average number of computational particles located in one grid cell at the initial time. The variable s is the distance along the surface measured from the leading edge.

VI. CONCLUSIONS

Based on the ES-FP model, which is a Fokker–Planck-type approximation of the gas-kinetic Boltzmann equation, stochastic particle simulation schemes for rarefied gas flows are developed. The conservation of momentum and energy can be numerically enforced in the ES-FP simulation by incorporating the following ideas into the algorithm: (1) decoupling of free-molecular moves and intermolecular collisions, (2) using instantaneous statistics to evaluate the macroscopic parameters that guide the particle evolution, and (3) correcting the particle velocities at the end of each time step.

The test case of homogeneous gas provides a direct and convincing evidence for the conservative property of the conservative ES-FP scheme. The simulations of two canonical flow problems in supersonic rarefied gas dynamics indicate the significance of this conservative property. A particle Fokker–Planck scheme without the enforcement of conservation laws may suffer from the following defects: (1) it is unable to maintain an undisturbed homogeneous macroscopic state; (2) it is sensitive to the average number of computational particles per cell; (3) it produces an unphysical low-temperature region in front of the shock wave; (4) it underestimates the shock angle and the shock standoff distance; (5) it makes inaccurate predictions of aerodynamic force and heating. For the examples considered here, the present conservative particle scheme can remedy these defects to a great extent.

Admittedly, the present conservative ES-FP scheme resembles the conventional DSMC method in the aspect of decoupling free-molecular moves and intermolecular collisions over each time step, and therefore, its conservative property is achieved at the expense of reducing the time step size Δt below the mean collision time τ_c of gas molecules. However, the original intention and the ultimate goal of the particle Fokker–Planck method is to permit arbitrarily large ratio of Δt to τ_c by coupling free-molecular moves and intermolecular collisions, which will fundamentally enhance the efficiency of the particle-based flow simulation. Hence, future investigations on the particle Fokker–Planck method should include the conservative implementations under the framework of coupled schemes.

ACKNOWLEDGMENTS

This research is supported by the Research Grants Council of Hong Kong (Grant No. GRF 152065/19E).

APPENDIX: PROOF OF MOMENTUM AND ENERGY CONSERVATION

Consider a computational cell that contains N particles inside. This section shows that the velocity evolution procedure according to Eq. (31) will satisfy the conservation of momentum [Eq. (35)] and the conservation of energy [Eq. (36)], as long as the macroscopic properties of this cell satisfy Eqs. (37) and (38) and the normal random vectors for particles in this cell satisfy Eqs. (39) and (40).

First, consider the proof of the momentum conservation Eq. (35). Multiply Eq. (31) by molecular mass m, and sum over all particles in the cell. As a result, one can get

$$\sum_{\text{pic}}[mc_i(t+\Delta t)] = \left(\sum_{\text{pic}} m\right)u_i + e^{-\Delta t/\tau}\left(\sum_{\text{pic}}[mc_i(t)] - \left(\sum_{\text{pic}} m\right)u_i\right) + \sqrt{mk_{\text{B}}T(1-e^{-2\Delta t/\tau})}L_{ik}\left(\sum_{n=1}^{N}\xi_k^{(n)}\right). \tag{A1}$$

Substituting Eqs. (37) and (39) into Eq. (A1) reproduces Eq. (35). This shows that the velocity evolution procedure conserves the momentum in the cell.

Then, consider the proof of the energy conservation Eq. (36). Using Eq. (31), one can get

$$\begin{aligned}\frac{1}{2}mc_i(t+\Delta t)c_j(t+\Delta t) &= \frac{1}{2}mu_iu_j + \frac{1}{2}u_je^{-\Delta t/\tau}[mc_i(t)-mu_i] + \frac{1}{2}u_ie^{-\Delta t/\tau}[mc_j(t)-mu_j]\\ &\quad + \frac{1}{2}e^{-2\Delta t/\tau}[mc_i(t)c_j(t) - u_jmc_i(t) - u_imc_j(t) + mu_iu_j]\\ &\quad + \frac{1}{2}k_{\text{B}}T(1-e^{-2\Delta t/\tau})L_{ik}L_{jm}\xi_k\xi_m.\end{aligned} \tag{A2}$$

Next, summing over all particles in the cell and utilizing Eqs. (37) and (40), one can get

$$\begin{aligned}\sum_{\text{pic}}\left[\frac{1}{2}mc_i(t+\Delta t)c_j(t+\Delta t)\right] &= \frac{1}{2}\left(\sum_{\text{pic}} m\right)u_iu_j + e^{-2\Delta t/\tau}\\ &\quad\times\left[\sum_{\text{pic}}\left[\frac{1}{2}mc_i(t)c_j(t)\right] - \frac{1}{2}\left(\sum_{\text{pic}} m\right)u_iu_j\right]\\ &\quad + \frac{1}{2}Nk_{\text{B}}T(1-e^{-2\Delta t/\tau})L_{ik}L_{jk}.\end{aligned} \tag{A3}$$

Note that matrix $\boldsymbol{L}$ is generated by the Cholesky decomposition of the tensor $\boldsymbol{E}$, and thus, $L_{ik}L_{jk}$ turns out to be E_{ij}. In addition, the definition of $\boldsymbol{E}$ [Eq. (5)] indicates that the trace of $\boldsymbol{E}$ is equal to 3. Therefore, by letting $i = j$, one can obtain

$$\begin{aligned}\sum_{\text{pic}}\left[\frac{1}{2}mc^2(t+\Delta t)\right] &= \frac{1}{2}\left(\sum_{\text{pic}} m\right)u^2 + e^{-2\Delta t/\tau}\\ &\quad\times\left[\sum_{\text{pic}}\left[\frac{1}{2}mc^2(t)\right] - \frac{1}{2}\left(\sum_{\text{pic}} m\right)u^2\right]\\ &\quad + N\left(\frac{3}{2}k_{\text{B}}T\right)(1-e^{-2\Delta t/\tau}).\end{aligned} \tag{A4}$$

By substituting Eq. (38) into Eq. (A4) and after some algebraic manipulations, Eq. (36) is derived. This shows that the velocity evolution procedure conserves the energy in the cell.

DATA AVAILABILITY

The data that support the findings of this study are available from the corresponding author upon reasonable request.

REFERENCES

[1]M. S. Ivanov and S. F. Gimelshein, "Computational hypersonic rarefied flows," Annu. Rev. Fluid Mech. **30**, 469–505 (1998).
[2]Z. Wang, L. Bao, and B. Tong, "Rarefaction criterion and non-Fourier heat transfer in hypersonic rarefied flows," Phys. Fluids **22**(12), 126103 (2010).
[3]I. D. Boyd, "Computation of hypersonic flows using the direct simulation Monte Carlo method," J. Spacecr. Rockets **52**(1), 38–53 (2015).
[4]T. E. Schwartzentruber and I. D. Boyd, "Progress and future prospects for particle-based simulation of hypersonic flow," Prog. Aerosp. Sci. **72**, 66–79 (2015).
[5]P. Nizenkov, M. Pfeiffer, A. Mirza, and S. Fasoulas, "Modeling of chemical reactions between polyatomic molecules for atmospheric entry simulations with direct simulation Monte Carlo," Phys. Fluids **29**, 077104 (2017).
[6]M. Schouler, Y. Prévereaud, and L. Mieussens, "Survey of flight and numerical data of hypersonic rarefied flows encountered in Earth orbit and atmospheric reentry," Prog. Aerosp. Sci. **118**, 100638 (2020).
[7]J. M. Reese, M. A. Gallis, and D. A. Lockerby, "New directions in fluid dynamics: Non-equilibrium aerodynamic and microsystem flows," Philos. Trans. R. Soc., A **361**, 2967–2988 (2003).
[8]M. Torrilhon, "Modeling nonequilibrium gas flow based on moment equations," Annu. Rev. Fluid Mech. **48**, 429–458 (2016).
[9]K. Kadau, J. L. Barber, T. C. Germann, B. L. Holian, and B. J. Alder, "Atomistic methods in fluid simulation," Philos. Trans. R. Soc., A **368**, 1547–1560 (2010).
[10]G. Karniadakis, A. Beskok, and N. Aluru, *Microflows and Nanoflows: Fundamentals and Simulation* (Springer, New York, USA, 2005).
[11]A. Agrawal, H. M. Kushwaha, and R. S. Jadhav, *Microscale Flow and Heat Transfer: Mathematical Modelling and Flow Physics* (Springer, Switzerland, 2020).
[12]X. Wang, T. Su, W. Zhang, Z. Zhang, and S. Zhang, "Knudsen pumps: A review," Microsyst. Nanoeng. **6**, 26–53 (2020).
[13]J. Zhang, S. Yao, F. Fei, M. Ghalambaz, and D. Wen, "Competition of natural convection and thermal creep in a square enclosure," Phys. Fluids **32**, 102001 (2020).
[14]M. Pfeiffer, "A particle-based ellipsoidal statistical Bhatnagar-Gross-Krook solver with variable weights for the simulation of large density gradients in micro- and nano-nozzles," Phys. Fluids **32**, 112009 (2020).
[15]C. Cercignani, *The Boltzmann Equation and its Application* (Springer, New York, USA, 1988).
[16]G. A. Bird, *Molecular Gas Dynamics and the Direct Simulation of Gas Flows* (Clarendon Press, Oxford, UK, 1994).
[17]G. A. Bird, *The DSMC Method* (CreateSpace Independent Publishing Platform, San Bernardino, USA, 2013).
[18]G. A. Bird, "Approach to translational equilibrium in a rigid sphere gas," Phys. Fluids **6**, 1518 (1963).
[19]S. F. Gimelshein and I. J. Wysong, "Bird's total collision energy model: 4 decades and going strong," Phys. Fluids **31**, 076101 (2019).
[20]S. Fasoulas, C.-D. Munz, M. Pfeiffer, J. Beyer, T. Binder, S. Copplestone, A. Mirza, P. Nizenkov, P. Ortwein, and W. Reschke, "Combining particle-in-cell and direct simulation Monte Carlo for the simulation of reactive plasma flows," Phys. Fluids **31**, 072006 (2019).
[21]S. J. Plimpton, S. G. Moore, A. Borner, A. K. Stagg, T. P. Koehler, J. R. Torczynski, and M. A. Gallis, "Direct simulation Monte Carlo on petaflop supercomputers and beyond," Phys. Fluids **31**, 086101 (2019).
[22]A. Frezzotti, P. Barbante, and L. Gibelli, "Direct simulation Monte Carlo applications to liquid-vapor flows," Phys. Fluids **31**, 062103 (2019).
[23]S. M. Longshaw, R. Pillai, L. Gibelli, D. R. Emerson, and D. A. Lockerby, "Coupling molecular dynamics and direct simulation Monte Carlo using a general and high-performance code coupling library," Comput. Fluids **213**, 104726 (2020).
[24]G. Cai, X. Ren, B. He, Z. Tang, and J. Yuan, "The dependence of transport coefficient on spatial dimensions and grid shape in the direct simulation Monte Carlo based on Green–Kubo relation," Phys. Fluids **32**, 042006 (2020).
[25]F. J. Alexander, A. L. Garcia, and B. J. Alder, "Cell size dependence of transport coefficients in stochastic particle algorithms," Phys. Fluids **10**, 1540–1542 (1998).
[26]A. L. Garcia and W. Wagner, "Time step truncation error in direct simulation Monte Carlo," Phys. Fluids **12**, 2621–2633 (2000).
[27]N. G. Hadjiconstantinou, "Analysis of discretization in the direct simulation Monte Carlo," Phys. Fluids **12**, 2634–2638 (2000).
[28]D. J. Rader, M. A. Gallis, J. R. Torczynski, and W. Wagner, "Direct simulation Monte Carlo convergence behavior of the hard-sphere-gas thermal conductivity for Fourier heat flow," Phys. Fluids **18**, 077102 (2006).
[29]R. S. Myong, A. Karchani, and O. Ejtehadi, "A review and perspective on a convergence analysis of the direct simulation Monte Carlo and solution verification," Phys. Fluids **31**, 066101 (2019).
[30]J. Zhang, B. John, M. Pfeiffer, F. Fei, and D. Wen, "Particle-based hybrid and multiscale methods for nonequilibrium gas flows," Adv. Aerodyn. **1**, 12 (2019).
[31]F. Fei and P. Jenny, "A hybrid particle approach based on the unified stochastic particle Bhatnagar-Gross-Krook and DSMC methods," J. Comput. Phys. **424**, 109858 (2021).
[32]P. Jenny, M. Torrilhon, and S. Heinz, "A solution algorithm for the fluid dynamic equations based on a stochastic model for molecular motion," J. Comput. Phys. **229**, 1077 (2010).
[33]M. H. Gorji, M. Torrilhon, and P. Jenny, "Fokker-Planck model for computational studies of monatomic rarefied gas flows," J. Fluid Mech. **680**, 574 (2011).
[34]M. H. Gorji and M. Torrilhon, "A Fokker–Planck model of hard sphere gases based on H-theorem," AIP Conf. Proc. **1786**, 090001 (2016).
[35]M. H. Gorji and M. Torrilhon, "Entropic Fokker–Planck kinetic model," Proc. R. Soc. London, Ser. A (submitted) (2019).
[36]S. K. Singh and S. Ansumali, "Fokker–Planck model of hydrodynamics," Phys. Rev. E **91**, 033303 (2015).
[37]S. K. Singh, C. Thantanapally, and S. Ansumali, "Gaseous microflow modeling using the Fokker–Planck equation," Phys. Rev. E **94**, 063307 (2016).
[38]J. Mathiaud and L. Mieussens, "A Fokker-Planck model of the Boltzmann equation with correct Prandtl number," J. Stat. Phys. **162**, 397–414 (2016).
[39]H. Gorji and P. Jenny, "A kinetic model for gas mixtures based on a Fokker-Planck equation," J. Phys.: Conf. Ser. **362**, 012042 (2012).
[40]S. Agrawal, S. K. Singh, and S. Ansumali, "Fokker-Planck model for binary mixtures," J. Fluid Mech. **899**, A25 (2020).
[41]C. Hepp, M. Grabe, and K. Hannemann, "A kinetic Fokker-Planck approach to model hard-sphere gas mixtures," Phys. Fluids **32**, 027103 (2020).
[42]C. Hepp, M. Grabe, and K. Hannemann, "A kinetic Fokker-Planck approach for modeling variable hard-sphere gas mixtures," AIP Adv. **10**, 085219 (2020).
[43]M. H. Gorji and P. Jenny, "A Fokker-Planck based kinetic model for diatomic rarefied gas flows," Phys. Fluids **25**, 062002 (2013).
[44]J. Mathiaud and L. Mieussens, "A Fokker-Planck model of the Boltzmann equation with correct Prandtl number for polyatomic gases," J. Stat. Phys. **168**, 1031–1055 (2017).
[45]J. Mathiaud and L. Mieussens, "BGK and Fokker-Planck models of the Boltzmann equation for gases with discrete levels of vibrational energy," J. Stat. Phys. **178**, 1076–1095 (2020).
[46]C. Hepp, M. Grabe, and K. Hannemann, "Master equation approach for modeling diatomic gas flows with a kinetic Fokker-Planck algorithm," J. Comput. Phys. **418**, 109638 (2020).
[47]M. Sadr and M. H. Gorji, "A continuous stochastic model for non-equilibrium dense gases," Phys. Fluids **29**, 122007 (2017).
[48]M. Sadr, M. Pfeiffer, and M. H. Gorji, "Fokker–Planck–Poisson kinetics: Multiphase flow beyond equilibrium," J. Fluid Mech. (submitted) (2020).
[49]M. H. Gorji and P. Jenny, "An efficient particle Fokker-Planck algorithm for rarefied gas flows," J. Comput. Phys. **262**, 325–343 (2014).
[50]M. Pfeiffer and M. H. Gorji, "Adaptive particle-cell algorithm for Fokker-Planck based rarefied gas flow simulations," Comput. Phys. Commun. **213**, 1–8 (2017).
[51]J. Zhang and J. Fan, "Two critical issues in Langevin simulation of gas flows," AIP Conf. Proc. **1628**, 1087–1094 (2014).
[52]T. Önskog and J. Zhang, "An accurate treatment of diffuse reflection boundary conditions for a stochastic particle Fokker-Planck algorithm with large time steps," Physica A **440**, 139–146 (2015).
[53]J. Zhang, D. Zeng, and J. Fan, "Analysis of transport properties determined by Langevin dynamics using Green-Kubo formulae," Physica A **411**, 104–112 (2014).

[54]F. Fei, Z. Liu, J. Zhang, and C. Zheng, "A multi-scale method for rarefied and continuum gas flows based on Fokker–Planck model," AIP Conf. Proc. **1786**, 180009 (2016).
[55]F. Fei, Z. Liu, J. Zhang, and C. Zheng, "A particle Fokker-Planck algorithm with multiscale temporal discretization for rarefied and continuum gas flows," Commun. Comput. Phys. **22**(2), 338–374 (2017).
[56]M. H. Gorji, N. Andric, and P. Jenny, "Variance reduction for Fokker-Planck based particle Monte Carlo schemes," J. Comput. Phys. **295**, 644–664 (2015).
[57]B. S. Collyer, C. Connaughton, and D. A. Lockerby, "Importance sampling variance reduction for the Fokker-Planck rarefied gas particle method," J. Comput. Phys. **325**, 116–128 (2016).
[58]P. Jenny, S. Küchlin, and H. Gorji, "Controlling the bias error of Fokker-Planck methods for rarefied gas dynamics simulations," Phys. Fluids **31**, 062005 (2019).
[59]F. Fei and J. Fan, "A diffusive information preservation method for small Knudsen number flows," J. Comput. Phys. **243**, 179–193 (2013).
[60]F. Fei, Z. Liu, and C. Zheng, "Statistical simulation of molecular diffusion effect on turbulent tetrad dispersion," Int. J. Heat Mass Transfer **103**, 87–98 (2016).
[61]M. H. Gorji and P. Jenny, "Fokker-Planck-DSMC algorithm for simulations of rarefied gas flows," J. Comput. Phys. **287**, 110–129 (2015).
[62]S. Küchlin and P. Jenny, "Parallel Fokker-Planck-DSMC algorithm for rarefied gas flow simulation in complex domains at all Knudsen numbers," J. Comput. Phys. **328**, 258–277 (2017).
[63]S. Küchlin and P. Jenny, "Automatic mesh refinement and parallel load balancing for Fokker-Planck-DSMC algorithm," J. Comput. Phys. **363**, 140–157 (2018).
[64]E. Jun, M. H. Gorji, M. Grabe, and K. Hannemann, "Assessment of the cubic Fokker-Planck-DSMC hybrid method for hypersonic rarefied flows past a cylinder," Comput. Fluids **168**, 1–13 (2018).
[65]C. Hepp, M. Grabe, and K. Hannemann, "Non-equilibrium parameter for a hybrid Fokker–Planck/DSMC scheme," AIP Conf. Proc. **2132**, 070002 (2019).
[66]Y. Jiang, Z. Gao, and C.-H. Lee, "Particle simulation of nonequilibrium gas flows based on ellipsoidal statistical Fokker-Planck model," Comput. Fluids **170**, 106–120 (2018).
[67]E. Jun, M. Pfeiffer, L. Mieussens, and M. H. Gorji, "Comparative study between cubic and ellipsoidal Fokker-Planck kinetic models," AIAA J. **57**(6), 2524–2533 (2019).
[68]M. Pfeiffer, A. Mirza, and P. Nizenkov, "Evaluation of particle-based continuum methods for a coupling with the direct simulation Monte Carlo method based on a nozzle expansion," Phys. Fluids **31**, 073601 (2019).
[69]K. Hannemann, C. Hepp, M. Grabe, and V. Hannemann, "Numerical analysis of re-entry configuration aerodynamics in the near continuum rarefied flow regimes," in *Proceedings of the 32nd International Symposium on Shock Waves* (Research Publishing, Singapore, 2019), pp. 1591–1601.
[70]F. Fei, H. Liu, Z. Liu, and J. Zhang, "A benchmark study of kinetic models for shock waves," AIAA J. **58**(6), 2596–2608 (2020).
[71]E. Jun, M. Grabe, and K. Hannemann, "Cubic Fokker-Planck method for rarefied monatomic gas flow through a slit and an orifice," Comput. Fluids **175**, 199–213 (2018).
[72]B. Xiao and R. Li, "Ellipsoidal statistical Fokker-Planck simulation of thermally induced gas flow in a ratchet microchannel," J. Phys.: Conf. Ser. **1168**, 032037 (2019).
[73]V. RezapourJaghargh, A. Mahdavi, and E. Roohi, "Shear-driven micro/nano flows simulation using Fokker Planck approach: Investigating accuracy and efficiency," Vacuum **172**, 109065 (2020).
[74]J. Zhang and T. Önskog, "Langevin equation elucidates the mechanism of the Rayleigh-Bénard instability by coupling molecular motions and macroscopic fluctuations," Phys. Rev. E **96**, 043104 (2017).
[75]J. Zhang, P. Tian, S. Yao, and F. Fei, "Multiscale investigation of Kolmogorov flow: From microscopic molecular motions to macroscopic coherent structures," Phys. Fluids **31**, 082008 (2019).
[76]S. Liu, R. Yuan, U. Javid, and C. Zhong, "Conservative discrete-velocity method for the ellipsoidal Fokker-Planck equation in gas-kinetic theory," Phys. Rev. E **100**, 033310 (2019).
[77]Y. Jiang, "Numerical study of gas flows spanning continuum and rarefied regimes," Ph.D. thesis, Beihang University, China, 2018.
[78]W. G. Vincenti and C. H. Kruger, Jr., *Introduction to Physical Gas Dynamics* (Krieger Publishing Company, Florida, USA, 1965).
[79]C. W. Gardiner, *Stochastic Methods: A Handbook for the Natural and Social Sciences* (Springer-Verlag, Berlin, Germany, 2009).
[80]N. G. Van Kampen, *Stochastic Processes in Physics and Chemistry* (Elsevier, Singapore, 2009).
[81]Y. Jiang, Z. Gao, C. Jiang, and C.-H. Lee, "Hypersonic aeroheating characteristics of leading edges with different nose radii," J. Thermophys. Heat Transfer **31**(3), 538–548 (2017).